Benchmark Shock Tube Experiments of Radiative Heating Relevant to Earth Re-entry

A. M. Brandis*†and B. A. Cruden‡
AMA at NASA Ames, Mountain View, CA, 94035, USA,

Detailed spectrally and spatially resolved radiance has been measured in the Electric Arc Shock Tube (EAST) facility for conditions relevant to high speed entry into a variety of atmospheres, including Earth, Venus, Titan, Mars and the Outer Planets. The tests that measured radiation relevant for Earth re-entry are the focus of this work and are taken from campaigns 47, 50, 52 and 57. These tests covered conditions from 8 km/s to 15.5 km/s at initial pressures ranging from 0.05 Torr to 1 Torr, of which shots at 0.1 and 0.2 Torr are analyzed in this paper. These conditions cover a range of points of interest for potential flight missions, including return from Low Earth Orbit, the Moon and Mars. The large volume of testing available from EAST is useful for statistical analysis of radiation data, but is problematic for identifying representative experiments for performing detailed analysis. Therefore, the intent of this paper is to select a subset of benchmark test data that can be considered for further detailed study. These benchmark shots are intended to provide more accessible data sets for future code validation studies and facility-to-facility comparisons. The shots that have been selected as benchmark data are the ones in closest agreement to a line of best fit through all of the EAST results, whilst also showing the best experimental characteristics, such as test time and convergence to equilibrium. The EAST data are presented in different formats for analysis. These data include the spectral radiance at equilibrium, the spatial dependence of radiance over defined wavelength ranges and the mean non-equilibrium spectral radiance (so-called "spectral non-equilibrium metric"). All the information needed to simulate each experimental trace, including free-stream conditions, shock time of arrival (i.e. x-t) relation, and the spectral and spatial resolution functions, are provided.

I. Introduction

In recent years, the EAST facility at NASA Ames has been employed for the purpose of obtaining validation data for radiative heating. The shock tube produces high velocity flows in gases of known composition and densities relevant to various atmospheric entries. These conditions are achieved by creating a sudden pressure discontinuity which moves hypersonically into the gas in front of it, in the form of a normal shock wave. Because of the short time scales involved, the discontinuity does not have time to mix, but rather compresses the gas as it moves forward, much like a spacecraft will do to the atmosphere during planetary entry. This shock wave in EAST is therefore assumed to be analogous to the stagnation line behind the bow shock in an entry scenario. The radiating shock wave can be imaged as it passes through the shock tube, and separated into different wavelength ranges via spectroscopy. The spectroscopic imaging of the shock is important as the radiation varies significantly with wavelength. The ability to predict and model both the non-equilibrium and equilibrium radiance is dependent upon understanding the mechanisms that produce different spectral features. For the simulation tools that are used to predict radiative heating for a re-entry vehicle; the shock tube data is used to quantify uncertainty and validate such predictive models, and in some cases to adjust or update the models.

*Senior Research Scientist, Aerothermodynamics Branch, and Senior Member AIAA.
†Contact: aaron.m.brandis@nasa.gov
‡Senior Research Scientist, Aerothermodynamics Branch, and Associate Fellow AIAA

II. Description of the EAST Facility

The EAST facility at NASA Ames Research Center was developed to simulate high-enthalpy, real gas phenomena encountered by hypersonic vehicles entering planetary atmospheres. Experiments are performed to match flow parameters relevant to flight, such as velocity, static pressure, and atmospheric composition. EAST has the capability of producing super-orbital shock speeds using an electric arc driver with a driven tube diameter of 10.16 cm.[1,2] The region of valid test gas is located between the shock front and the contact surface that separates the driver and driven gases. The test duration is defined as the axial distance between these two points divided by the local shock velocity. The characteristics of the EAST arc driver result in test durations of approximately 4 - 10 μs. Though short, this test duration is often sufficient to capture the peak non-equilibrium shock radiation and the decay to equilibrium conditions. Spectrometers, attached to Charge Coupled Devices (CCDs) are activated when the shocked gas arrives at the location of the test section in the tube and the spectral and spatial emission of the gas are measured. EAST utilizes four spectrometers per shot, each associated with four different wavelength ranges. These cameras are referred to as: VUV ($\sim$ 120 – 215 nm), UV/Vis ($\sim$ 190 nm – 500 nm), Vis/NIR ($\sim$ 480 nm – 900 nm), and IR ($\sim$ 700 nm – 1650 nm).

II.A. Test Conditions

Figure 1 shows a comparison of EAST testing conditions with various flight missions that re-entered Earth's atmosphere and proposed Mars return missions. Four sets of EAST data are shown, denoted Test 47,[1] 50,[3,4] 52[5] and 57.[6] The nominal test conditions for Tests 47 and 50 were chosen to be representative of peak heating for the Multi Purpose Crew Vehicle's (MPCV's) re-entry into Earth's atmosphere during a lunar return mission. These conditions correspond to a shock speed of approximately 10 km/s to 10.5 km/s, free stream pressures ranging from 0.1 Torr to 1 Torr[3,4] and a test gas composition of 79% N_2 and 21% O_2 by mole (an idealized approximation of Earth's atmosphere). However, in order to better ascertain the dependency of the radiation with shock speed, shots were aimed at expanding the testing conditions to encompass speeds from 8 km/s up to 15.5 km/s, e.g. Test 50 (for shock speeds down to 8 km/s) and Test 52 (for shock speeds up to 15.5 km/s). This expanded data-set provided a more complete picture to analyze the relationship between shock speed and emitted radiation and allowed for a more robust comparison with simulations. Test 57 conducted experiments with an actual air mixture of 78.1% N_2, 20.9% O_2, 0.9% Ar along with trace species. Data from these tests may be obtained by contacting the authors or visiting the EAST data storage website (https://data.nasa.gov/docs/datasets/aerothermodynamics/EAST/index.html).

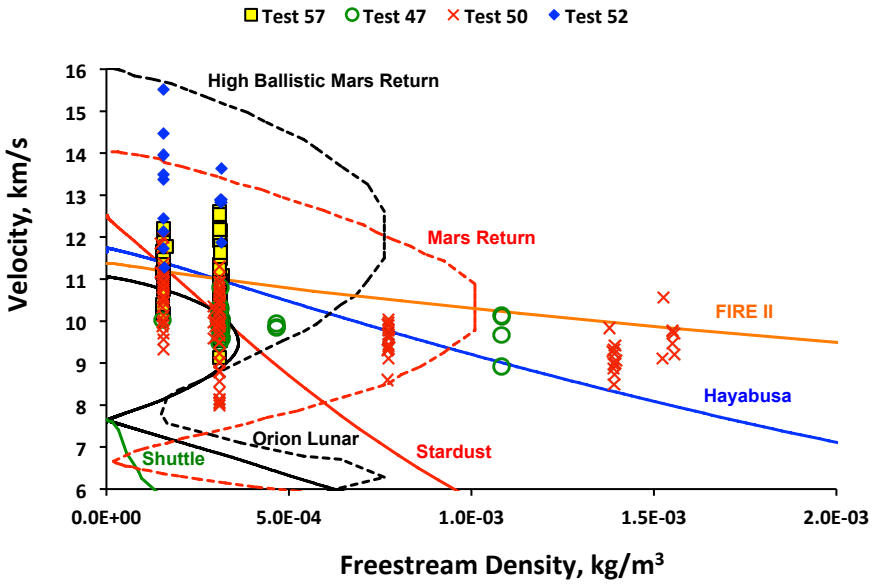

Figure 1. Comparison of EAST testing conditions to various flight missions that re-entered Earth's atmosphere and proposed Mars return missions.

III. Summary of Previous Research

There have been many research efforts in recent years to validate and analyze the EAST experiments.[3–12] Some of these previous analyses[4,6] have helped identify the benchmark EAST experiments. The following sections will provide an overview of these works with regard to analysis of both equilibrium and non-equilibrium radiation.

III.A. Summary of Previous Equilibrium Research

A previous analysis presented simulations of equilibrium radiation measurements obtained in the EAST as a part of recent testing aimed at reaching shock velocities up to 15.5 km/s.[4,5] The goal of these experiments was to measure the level of radiation encountered during high speed Earth entry conditions. These experiments provided spectrally and spatially resolved data for conditions ranging from 8 to 15.5 km/s at 0.1 and 0.2 Torr. Insights into the agreement between experimental results and simulations (NEQAIR[13,14] and HARA[15,16]) were made possible by analyzing integrated equilibrium spectra across a wide range of conditions and conducting detailed comparisons of the resulting trends.[4,5] The results showed that there was generally excellent agreement between the two codes and EAST data for the UV through IR spectral regions, however, discrepancies were identified in the VUV. It was concluded that an updated parametric uncertainty for high speed radiation in air was [9.0%, -6.3%]. Furthermore, due to the nature of the radiating environment at these high shock speeds, data were presented for phenomena that become increasingly significant with increasing shock speed. These investigations include analyzing the radiating species emitting ahead of the shock and the increased significance of radiative cooling mechanisms. Results from this work helped identify benchmark EAST shots based on the quality of the level of equilibrium radiation measured.

III.B. Non-equilibrium Metrics

For non-equilibrium regions of EAST experiments, a previously defined absolute non-equilibrium metric[17] is used to identify benchmark shots, and also used to provide non-equilibrium spectral data. This metric is computed by integrating the radiance within 2 cm of either side of the shock front, as shown by the red lines in Fig. 2, and is normalized by the shock tube diameter. For most cases, the shock front is defined as the location of peak radiance. For higher speed/pressure shots that do not over-shoot equilibrium, the location is chosen to be the inflection in the radiance as equilibrium is reached. Computing the metric in this manner has been suggested as a more robust way to conduct a comparison as opposed to using the peak intensity, since the comparisons are then not bound to experimental resolution limitations such as gate opening times and spatial smearing due to shock movement. Under optically thin conditions, this integral will represent the radiance as observed parallel to the direction of the shock. Under optically thick conditions, however, this integral is not physically meaningful and is simply a way of comparing data corresponding to a given optical path-length/shock tube diameter.

III.C. Summary of Previous Non-equilibrium Research

For lunar return Earth re-entry velocities between 8 and 11.5 km/s at 0.2 Torr, similar analyses as were performed for equilibrium were also conducted for non-equilibrium.[6] The experiments were aimed at measuring the spatially and spectrally resolved radiance at entry conditions for an approximate Earth atmosphere (79% N_2 : 21% O_2 by mole) and a more accurate composition featuring trace species (78.1% N_2 : 21.0% O_2 : 0.93% Ar by mole). Independent simulations were conducted with two sets of CFD and radiation codes (LAURA.[18,19]/HARA[15,16] and DPLR[20–22]/NEQAIR[13,14]), then compared to the EAST results using non-equilibrium metrics. Overall, LAURA/HARA was shown to under-predict EAST by as much as 40% and over-predict by as much as 12% depending on the shock speed. DPLR/NEQAIR was shown to under-predict EAST by as much as 50% and over-predict by as much as 20% depending on the shock speed. The one standard deviation scatter in the non-equilibrium EAST results was calculated to be 31%. Results from this work helped identify benchmark EAST shots based on the non-equilibrium metric analysis.

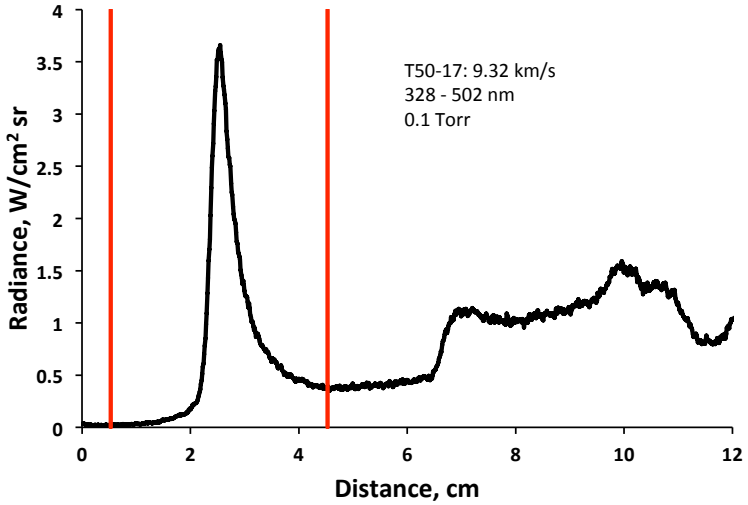

Figure 2. Example of the Absolute Non-equilibrium radiance metric used in this work: Integrating the intensity from 2 cm before the shock peak until 2 cm after the shock peak.

IV. Convolution Functions

In order to accurately model the EAST data, simulation results need to be spectrally and spatially convolved with functions which represent various sources of smearing intrinsic to the experimental set up. A detailed explanation for the determination of these parameters was previously published,[17] so a summary is presented here.

IV.A. Spectral Convolution Function

Every spectrometer has a spectral broadening function known as the Instrument Lineshape, ILS. The ILS is determined by the profile of radiation falling on the CCD coupled with the charge spread function of the CCD. The profile of the radiation falling on the CCD will be determined by the radiation profile passing through the spectrometer slit coupled with the spread function of the spectrometer optics. This spread function is also dependent upon the alignment (i.e. focus) of the CCD to the spectrometer. The EAST ILS was parameterized for ease of implementation in simulation tools.[4] The lineshape is determined experimentally by measuring and fitting atomic lines found in the emission from a spectral calibration lamp. The shape of the line is a function of several parameters, including the spectrometer, camera, slit width, grating resolution, wavelength setting and focus. Often the spectrometer CCD focus plays a larger role in determining lineshape than repeatable parameters such as slit width and grating angle, therefore the lineshape may drift over time and experience noticeable changes when realignment is performed. With the exception of the IR camera, the experimentally observed lineshapes are not well described by typical functions, such as triangular, Gaussian, Lorentzian or Voigt. Consequently, two empirical functions were created to better characterize the ILS; 1) the square root of a Voigt function (see Equation 1) and 2) a combination of a Gaussian and Lorentzian (see Equation 2). They are expressed mathematically as follows:

$$I(x) = (V(x))^{\frac{1}{2}} \tag{1}$$

where $V(x)$ is a Voigt Function and x is the wavelength separation from the line center. This function is described by two parameters, the Gaussian and Lorentzian widths that go into the Voigt Function.

$$I(x) = \frac{G(x) + a \times L(x)}{1 + a} \tag{2}$$

where $G(x)$ and $L(x)$ are Gaussian and Lorentzian functions and again x is the wavelength separation from the line center. This function requires three parameters, the Gaussian and Lorentzian line widths and the ratio a. Here, a is constrained between 0 and 1.

Depending on the specific set-up and settings used, one of the functions may provide a better fit to the spectral calibration lamp than the other. For each experimental condition, an ILS of either form is obtained,

however which form is used in the analysis is of little consequence as the functions are normalized to conserve the area under the curve. The integrated radiance is thus unaffected by this choice. The impact of the choice of the scan function is shown for calibration images in Fig. 3. Here, the camera signal is displayed as counts (summed over rows) on a logarithmic scale to highlight the spread of the ILS at low intensities far from the line center. Also shown for comparison is the best fit Voigt profile for the scan function. It is apparent that the Voigt profile is inadequate to capture the shape of the line wings. Gaussian or triangular functions would be even worse. The two proposed profiles, however, better capture the slow decay of intensity away from the line center. The parameters for the spectral resolution function are given in Appendix C.

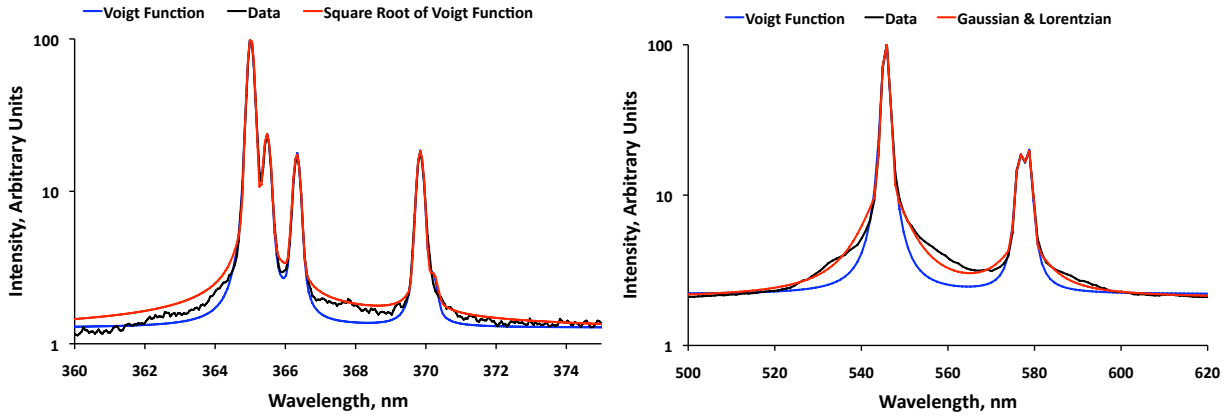

Figure 3. Measurement of Hg calibration lamp for the (a) VUV and (b) Vis/NIR spectrometers. Shown overlaid on the plots are the best fit instrument and Voigt functions. The instrument functions are defined in the text.

IV.B. Spatial Convolution Function

The spatial resolution of the experiments is restrained by physical limitations and arises from three different sources.[23] First, the resolution of both the collection and spectrometer optics will limit how finely the shock can be resolved. Second, the CCD itself is subject to charge smearing which will cause adjacent pixels to share intensity. Finally, the fact that the shock is moving during the exposure time will cause the shock front to blur on the camera. The first effect may be observed by taking the derivative of a step change in radiance, (e.g. at the edge of a sharply defined calibration source). It is found that the derivatives on the ICCD arrays are well fit by the square root of a Voigt function, which was also used to describe the spectral lineshape.[23] The net effect of the three resolution limitations results in a spatial profile that is broadened in comparison to the physical result. The broadening may be evaluated by convolving predicted data with an instrument spatial resolution function, SRF, which is itself a convolution of the optical, camera and motion resolution functions:

$$\begin{aligned} I_{meas}(x) &= \int_{-\infty}^{+\infty} SRF(\Delta x) I_{true}(x+\Delta x) d\Delta x \\ &= SRF(x) \otimes I_{true}(x) \\ SRF(x) &= f_{opt}(x) \otimes f_{cam}(x) \otimes f_{motion}(x) \end{aligned} \tag{3}$$

Taking an example of the three functions discussed above, a sample convolution function is given in Fig. 4, alongside the three individual functions. In this case, it is clear that the optical function is narrower than the camera and motion functions, which have comparable widths. However, since the camera function extends over a larger distance, it tends to dominate the convolution. These convolution functions have been compiled for the EAST data sets[23] and detailed in Appendix D.

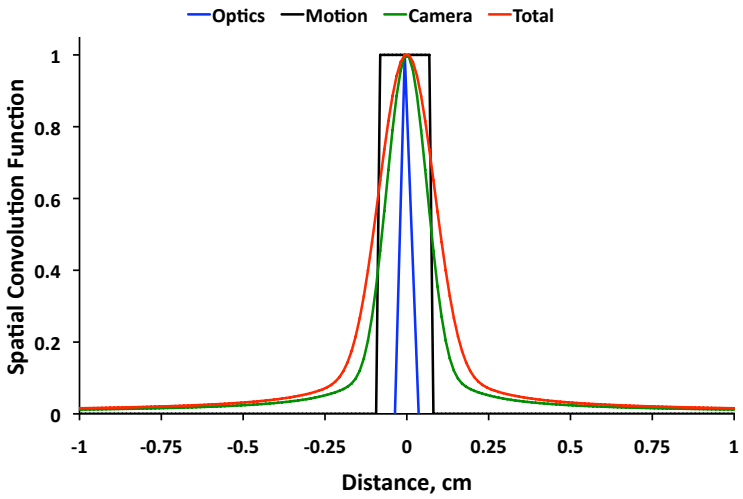

Figure 4. Sample convolution for the Vis/NIR Camera

V. Experimental Data

In order to identify benchmark EAST shots, the absolute non-equilibrium metric and equilibrium radiance was evaluated for each camera for each shot across test campaigns 47, 50, 52 and 57. A line of best fit to the data was created. Supposing the data to be normally distributed about this line, the shots showing the least deviation from the fit are selected as benchmark candidates. The results were then cross checked to find shots that showed favorable agreement across both the non-equilibrium and equilibrium fits. Tables 1 and 2 provide a listing of all the shots that were determined to be benchmark quality. Even though results from a shot might only specifically call out one camera as benchmark data, it does not mean that results from the other cameras did not provide useful data. These results from other cameras of benchmark shots might have only been slightly further off than another shot that was selected.

There were a few instances where additional selection criteria were necessary. Due to the scatter of the equilibrium results for the VUV camera at 0.1 Torr, the non-equilibrium metric was given precedence in selecting the benchmark cases. The non-equilibrium metric is also given precedence for shots less than approximately 10 km/s due to concerns about the level of equilibration obtained in EAST at such conditions. Figure 5 shows results from a previous analysis (Figs. 7, 9, 11, 13, 15)[3] that extracted electron number density by measuring the broadening of certain atomic lines. The results below approximately 10 km/s show that the extracted electron number density is significantly greater than equilibrium predictions. Shots with a low signal-to-noise ratio (typically VUV and IR at low speed), tended to have distorted non-equilibrium metrics due to noise or baseline offset in the pre-shock region. In these cases, the non-equilibrium metric was not considered.

Figures 6 to 15 show the benchmark EAST experiments across the four spectrometers typically used during each EAST experiment. Five spectral ranges are given, which include Deep VUV (117-175 nm, Figs. 6–7), VUV (122-180 nm, Figs. 8–9), UV/Vis (300-500 nm, Figs. 10–11), Vis/NIR (500-890 nm, Figs. 12–13) and IR (890-1450 nm, Figs. 14–15). The figures are displayed using the same layout for each spectral range. The radiance profile for the benchmark shots at 0.2 Torr and 0.1 Torr are shown first. In each case, one of the two ranges is shown as two separate figures in order to encompass a wider range of shock speeds. The benchmark shots are then highlighted on plots of equilibrium radiance and non-equilibrium metric verses shock speed for all shots considered in this analysis. The spectral dependence of both equilibrium radiance and the non-equilibrium metric are given in Appendix A. Appendix C and D gives the parameters necessary to produce the convolution functions discussed in Section IV for each test. Appendix B gives the distance-time data for each shock, which may be used for validation of CFD analyses of the full facility. Because the shock decelerates as it travels down the tube, this information is likely relevant for predicting the state of the shocked gas. This effect has been discussed previously as a possible reason for measured temperatures exceeding equilibrium for Mars entry relevant shots[24] and electron number densities above equilibrium in Air,[3] see Fig. 5.

Table 1. Benchmark EAST Shots at 0.1 Torr.

Test Series	Shot Number	Shock Speed km/s	Freestream Pressure Torr	Camera
50	17	9.32	0.1	UV/Vis
50	102	9.71	0.1	Vis/NIR
50	104	10.13	0.1	Vis/NIR
57	22	10.17	0.1	VUV
50	115	10.44	0.1	VUV
50	27	10.87	0.1	UV/Vis
50	106	10.97	0.1	Vis/NIR
50	20	11.11	0.1	VUV
57	34	11.15	0.1	VUV
50	105	11.26	0.1	Vis/NIR
52	1	11.27	0.1	UV/Vis,IR
57	25	11.67	0.1	Vis/NIR
52	2	11.72	0.1	UV/Vis, IR
50	24	11.74	0.1	VUV
50	107	11.86	0.1	VUV
52	5	12.45	0.1	UV/Vis
52	7	13.36	0.1	IR
52	8	13.5	0.1	UV/Vis,Vis/NIR
52	13	14.46	0.1	Vis/NIR
52	15	15.52	0.1	UV/Vis,Vis/NIR,IR

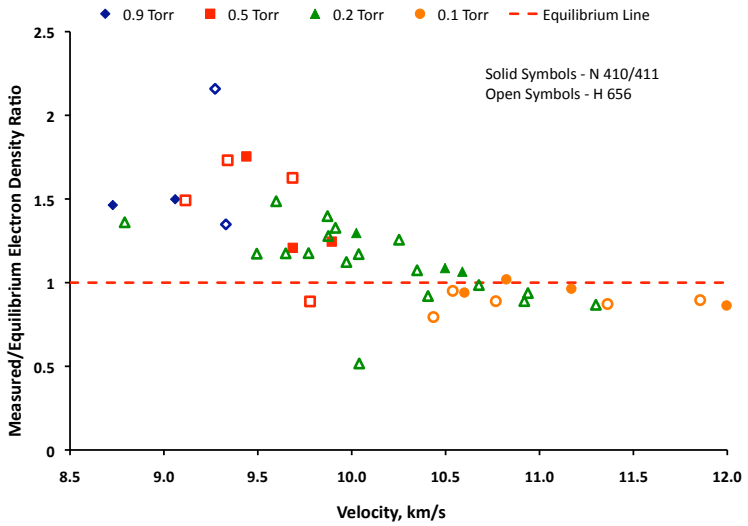

Figure 5. Ratio of measured electronic number density through Stark broadening and equilibrium calculated values as a function of velocity and pressure (adapted from Cruden et al.[3])

Table 2. Benchmark EAST Shots at 0.2 Torr.

Test Series	Shot Number	Shock Speed km/s	Freestream Pressure Torr	Camera
50	44	8.05	0.2	Vis/NIR
50	36	9.02	0.2	UV/Vis
57	14	9.53	0.2	VUV
50	59	9.98	0.2	UV/Vis,IR
57	15	10.12	0.2	VUV
57	6	10.13	0.2	Deep VUV
50	57	10.25	0.2	IR
47	37	10.27	0.2	Vis/NIR
50	29	10.29	0.2	VUV,UV
57	16	10.3	0.2	VUV
47	33	10.32	0.2	UV/Vis
57	7	10.44	0.2	Deep VUV
57	8	10.66	0.2	Deep VUV, IR
50	93	10.68	0.2	VUV
50	97	10.81	0.2	IR
50	30	10.92	0.2	Vis/NIR
57	41	11.22	0.2	UV/Vis
57	10	11.36	0.2	IR
57	11	11.50	0.2	Deep VUV
57	37	11.79	0.2	VUV,Vis/NIR
52	19	11.88	0.2	IR
57	40	12.19	0.2	UV/Vis
57	36	12.53	0.2	VUV
52	21	12.87	0.2	IR
52	20	12.89	0.2	Vis/NIR

The majority of the EAST experiments relevant to Earth entry have been conducted between approximately 10 and 12 km/s. Due to the large number of experiments in this shock speed range there is increased confidence in identifying benchmark shots close to the line of best fit. However, due to the relatively low number of shots outside of this range, the line of best fit can be influenced by just a few experiments. Care has been taken to select the best shots available in such cases, even if they have been selected from a small sample size. Furthermore, certain wavelength ranges have fewer experiments. This is true, for instance, of the deep VUV range (starting at 117 nm).

VI. Conclusion

This paper has examined the substantial number of experiments relevant to high speed Earth re-entry performed during recent campaigns in the EAST facility. Experiments that showed good shot characteristics, and agreed well with lines of best fit through the non-equilibrium metric and equilibrium radiance, were identified as benchmark datasets. As such, this work represents an archival distillation of the best experiments for recent EAST testing, covering tests 47, 50, 52 and 57. Detailed information has been provided for these experiments so they may be recreated by simulation tools, used in validation studies, or replicated by other facilities. Distance-time data for the shock traveling down the facility have also been included for the use in validation of future full facility CFD simulations. All of the EAST data is available at the following website: (https://data.nasa.gov/docs/datasets/aerothermodynamics/EAST/index.html).

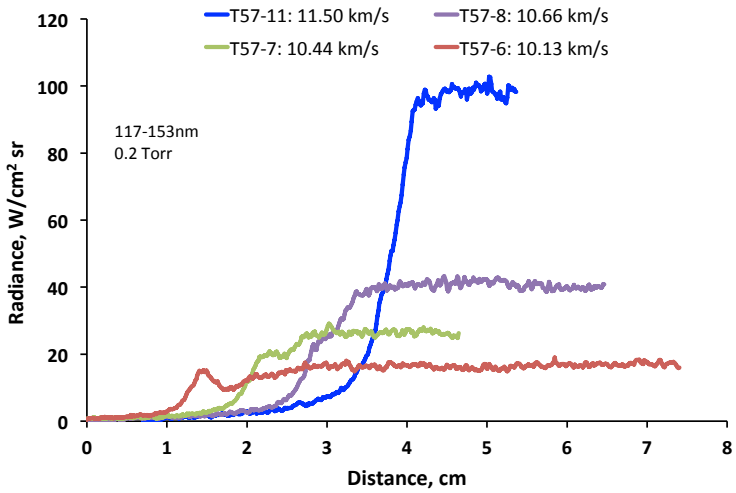

Figure 6. Deep VUV EAST data.

Acknowledgments

The authors would like to thank NASA's Entry Systems Modeling project for their support of this work. Drs Aaron Brandis and Brett Cruden are supported through the NNA15BB15C contract between NASA Ames Research Center and AMA Inc.

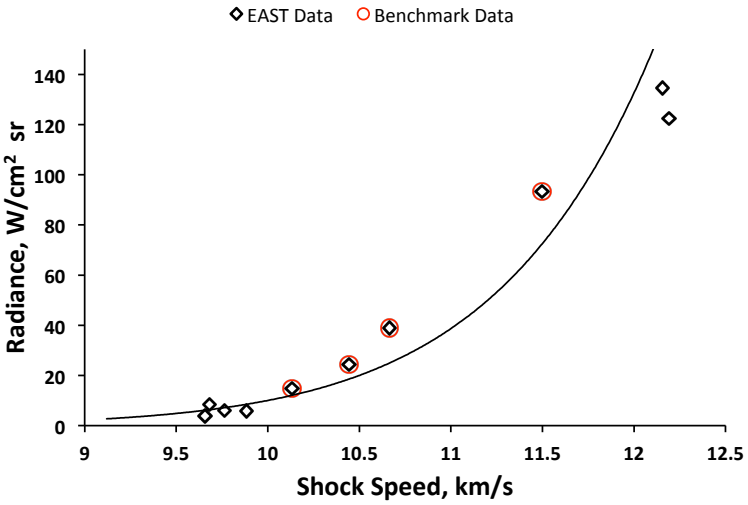

(a) Equilibrium

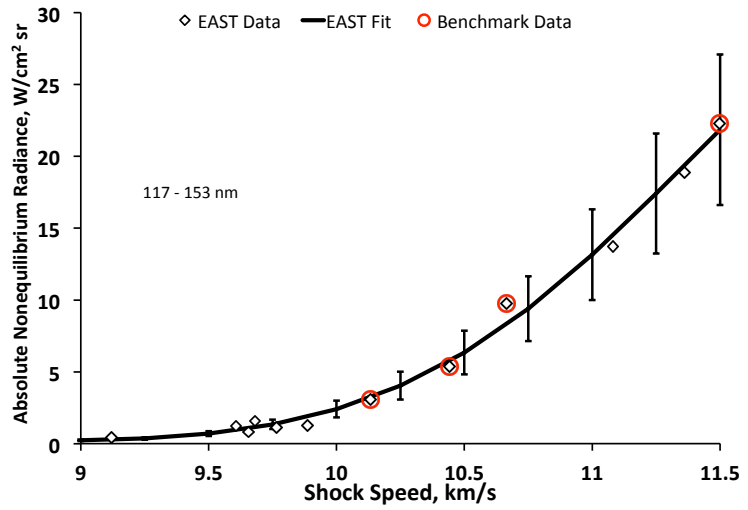

(b) Non-Equilibrium Metric at 0.2 Torr

Figure 7. Deep VUV EAST data.

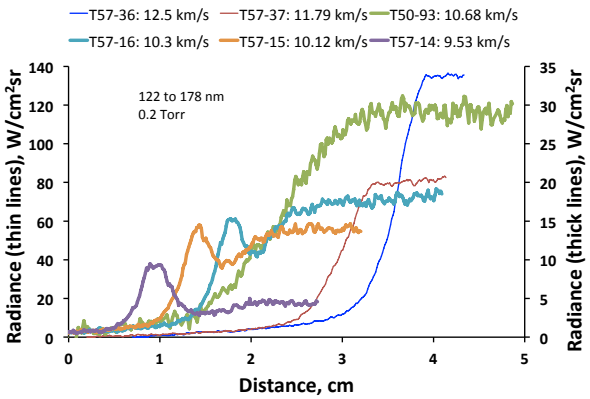

(a) Radiance Profiles at 0.2 Torr

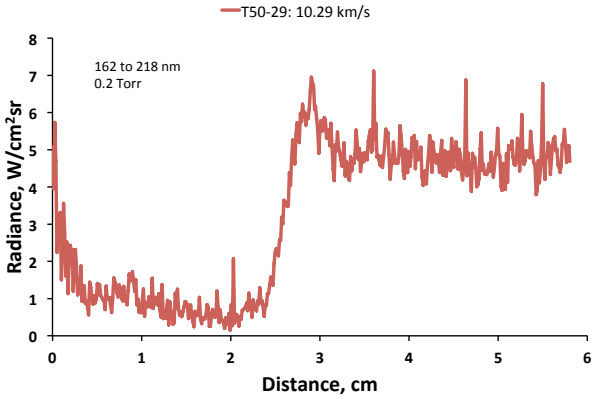

(b) Radiance Profiles at 0.2 Torr

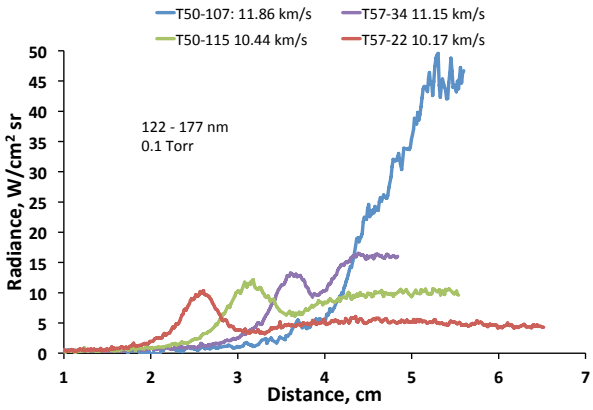

(c) Radiance Profiles at 0.1 Torr

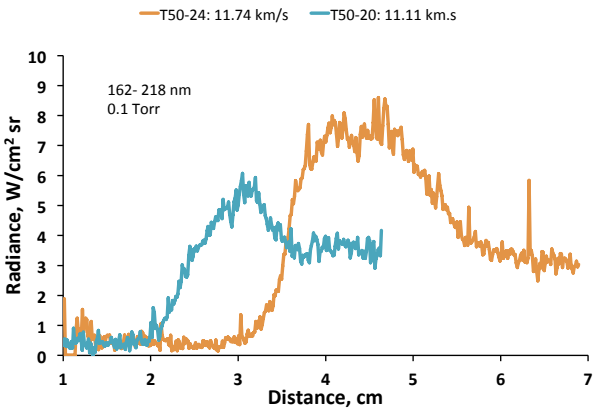

(d) Radiance Profiles at 0.1 Torr

Figure 8. VUV EAST data.

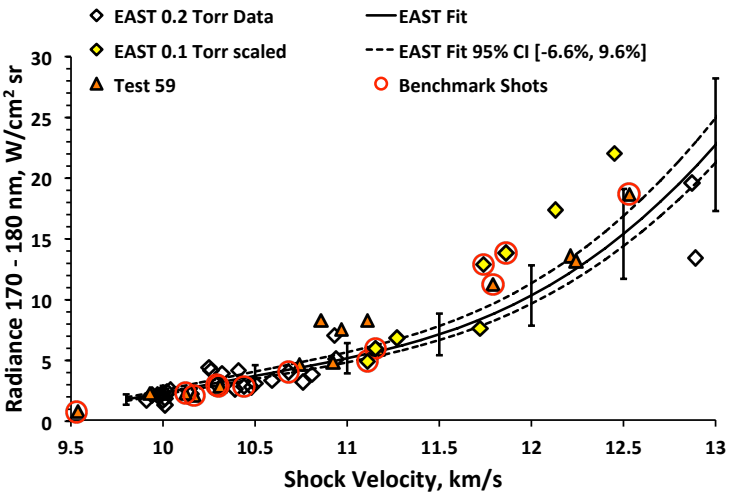

(a) Equilibrium

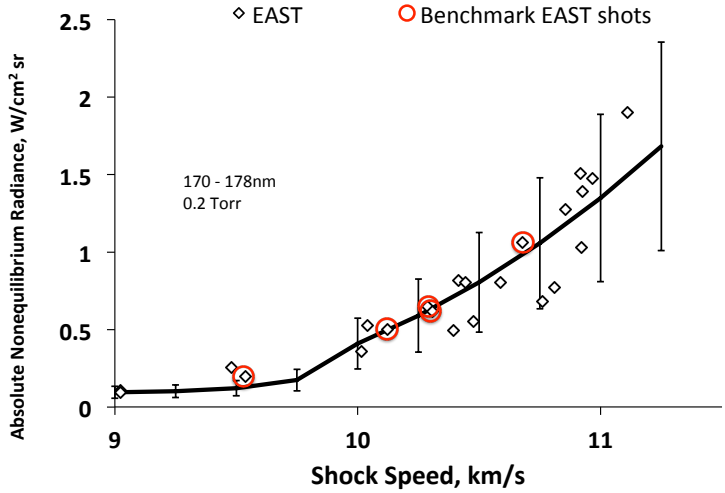

(b) Non-Equilibrium Metric at 0.2 Torr

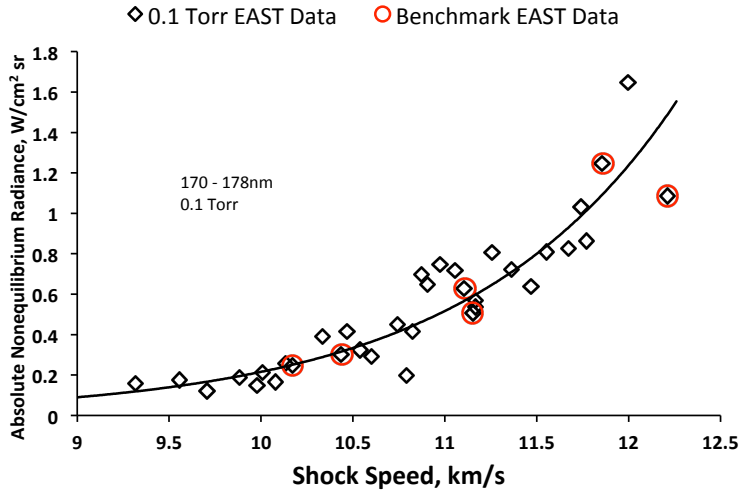

(c) Non-Equilibrium Metric at 0.1 Torr

Figure 9. VUV EAST data.

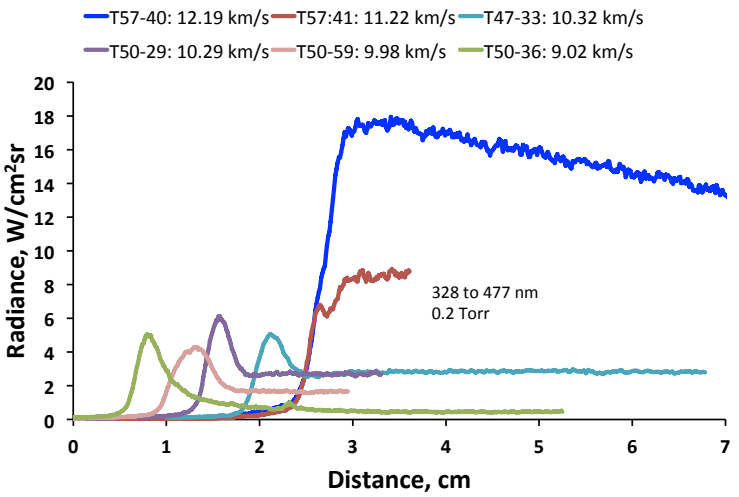

(a) Radiance Profiles at 0.2 Torr

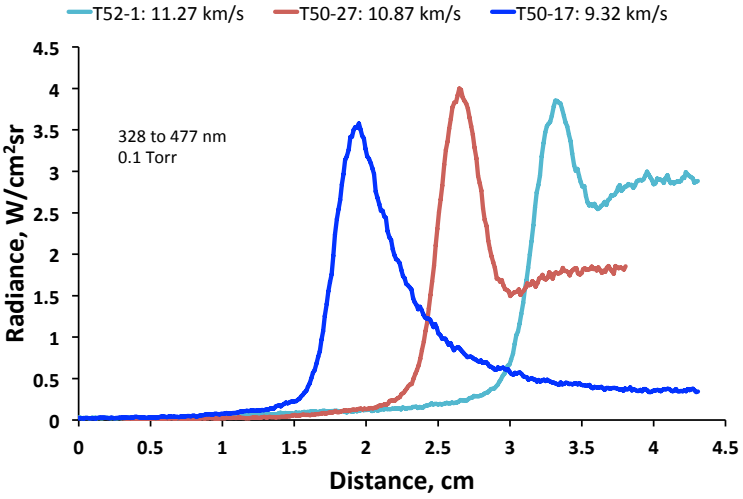

(b) Radiance Profiles at 0.1 Torr

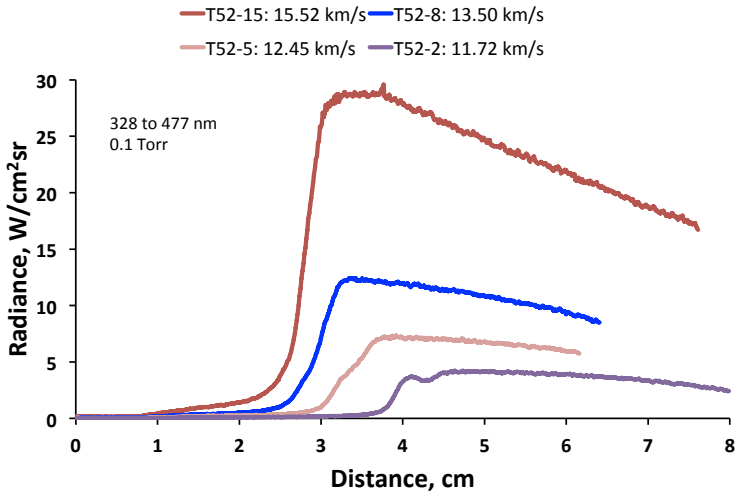

(c) Radiance Profiles at 0.1 Torr

Figure 10. UV EAST data.

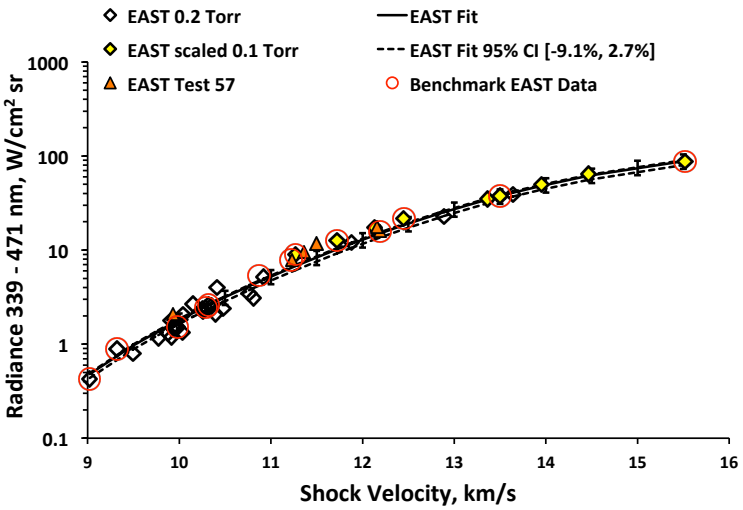

(a) Equilibrium

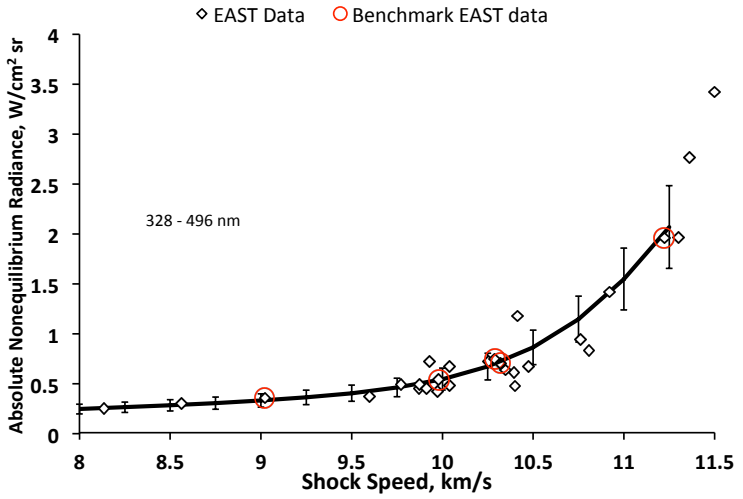

(b) Non-Equilibrium Metric at 0.2 Torr

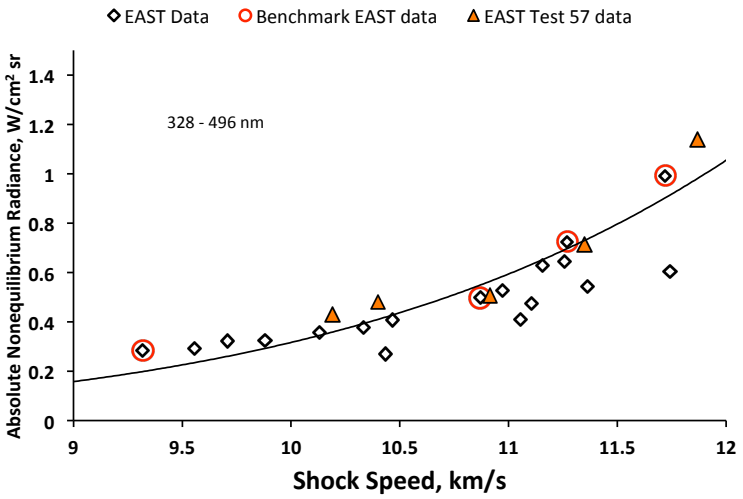

(c) Non-Equilibrium Metric at 0.1 Torr

Figure 11. UV EAST data.

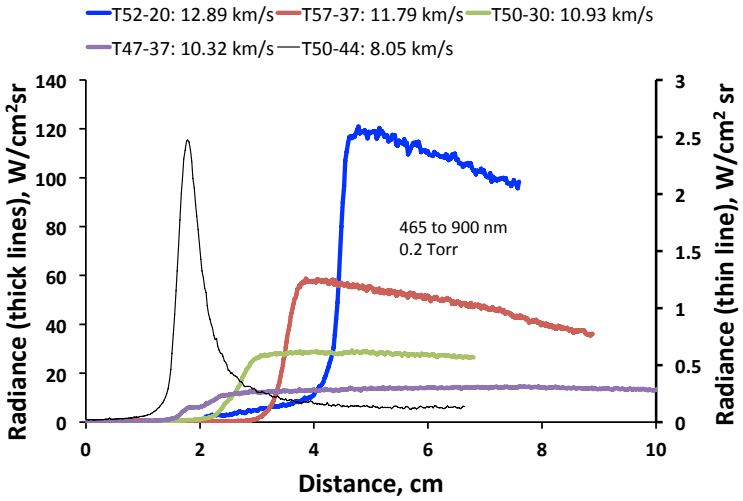

(a) Radiance Profiles at 0.2 Torr

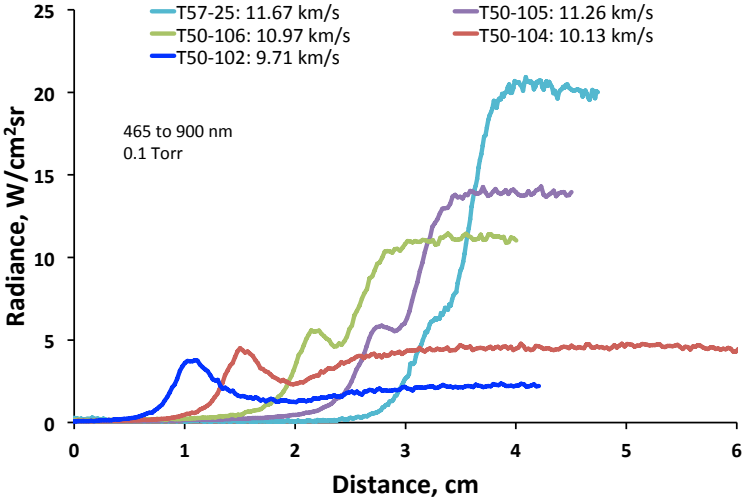

(b) Radiance Profiles at 0.1 Torr

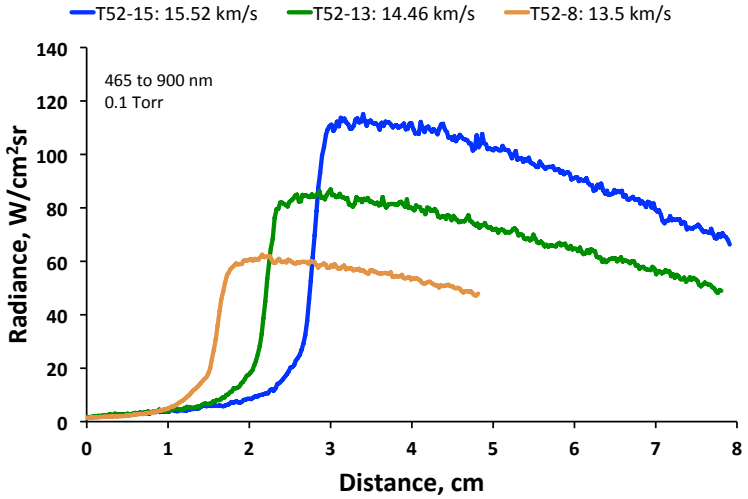

(c) Radiance Profiles at 0.1 Torr

Figure 12. Vis/NIR EAST data.

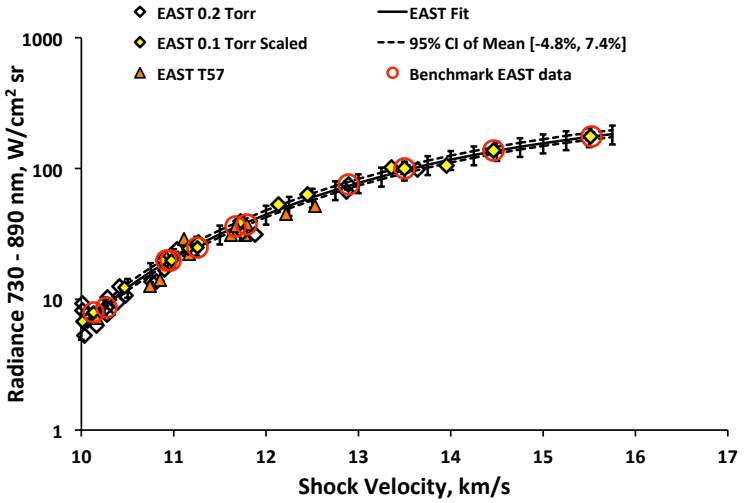

(a) Equilibrium

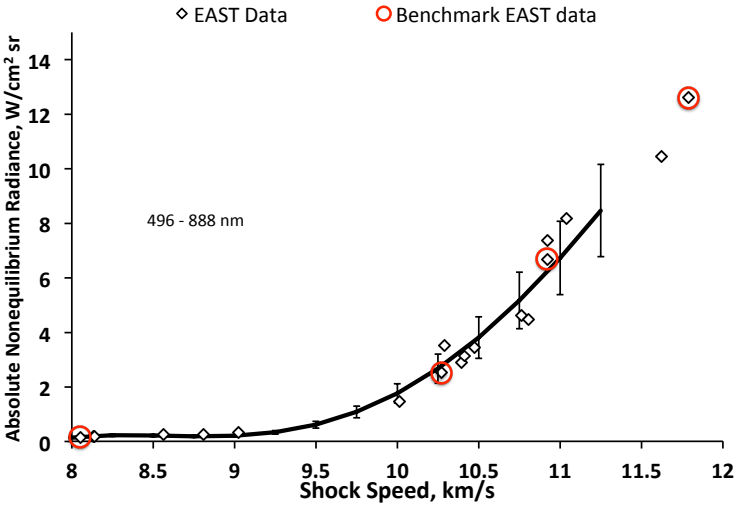

(b) Non-Equilibrium Metric at 0.2 Torr

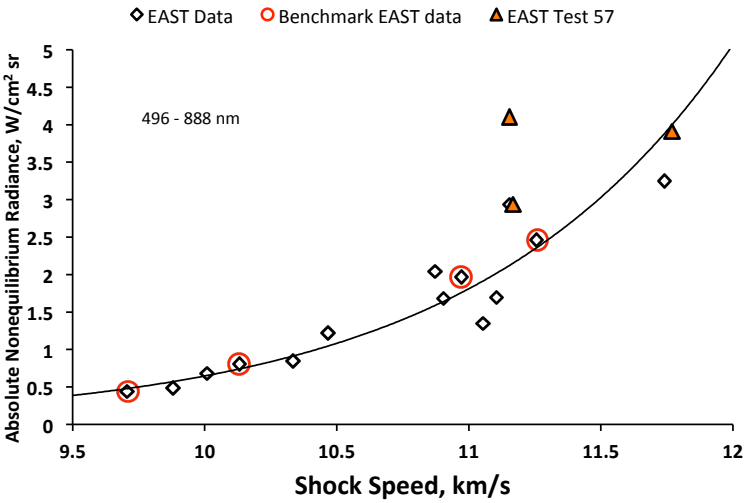

(c) Non-Equilibrium Metric at 0.1 Torr

Figure 13. Vis/NIR EAST data.

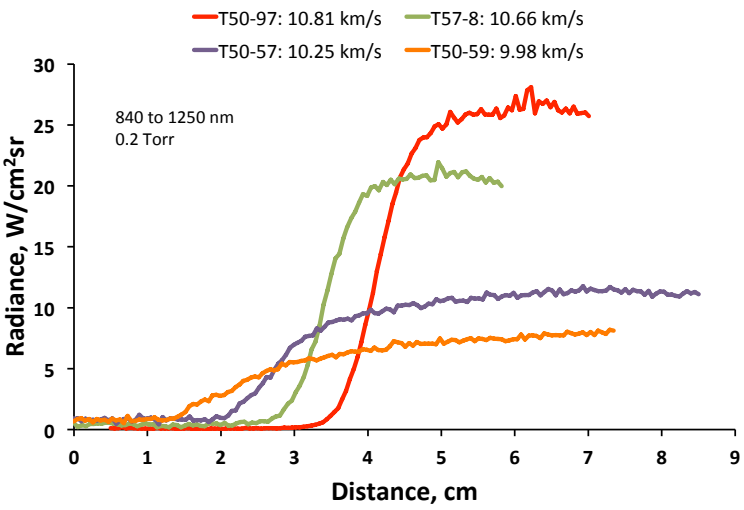

(a) Radiance Profiles at 0.2 Torr

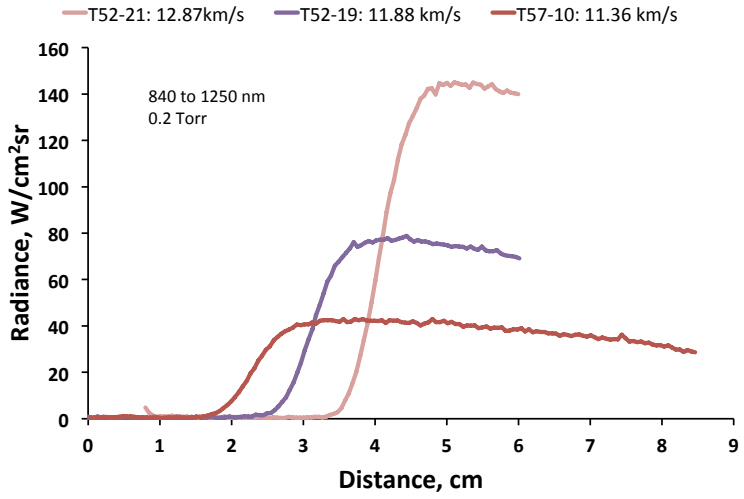

(b) Radiance Profiles at 0.2 Torr

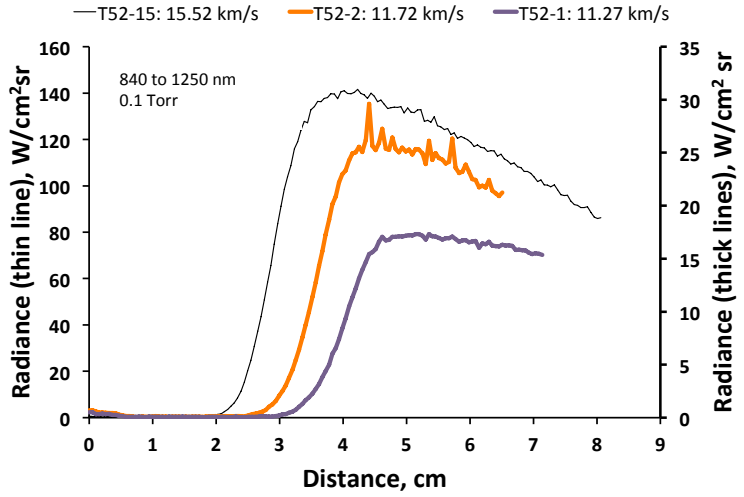

(c) Radiance Profiles at 0.1 Torr

Figure 14. IR EAST data.

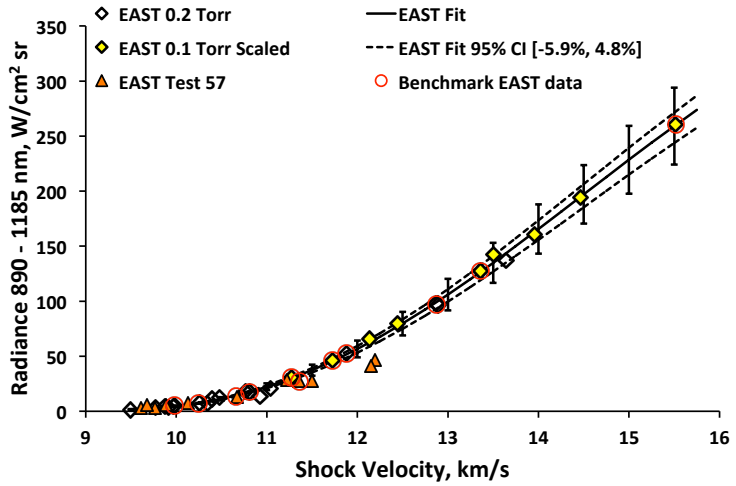

(a) Equilibrium

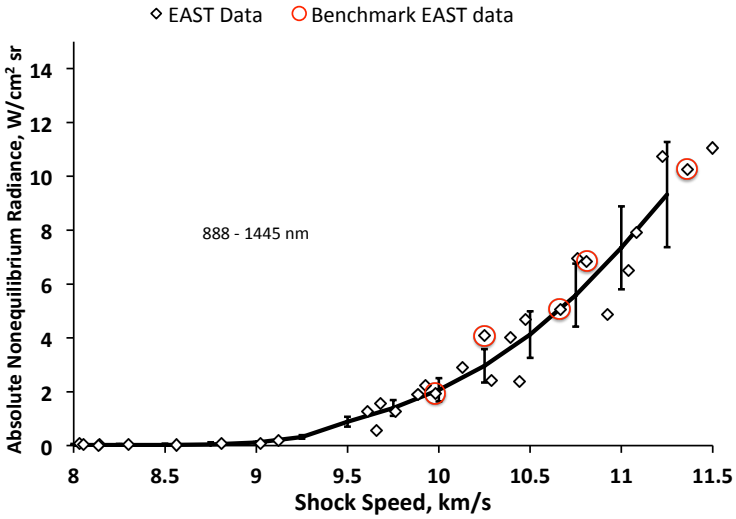

(b) Non-Equilibrium Metric at 0.2 Torr

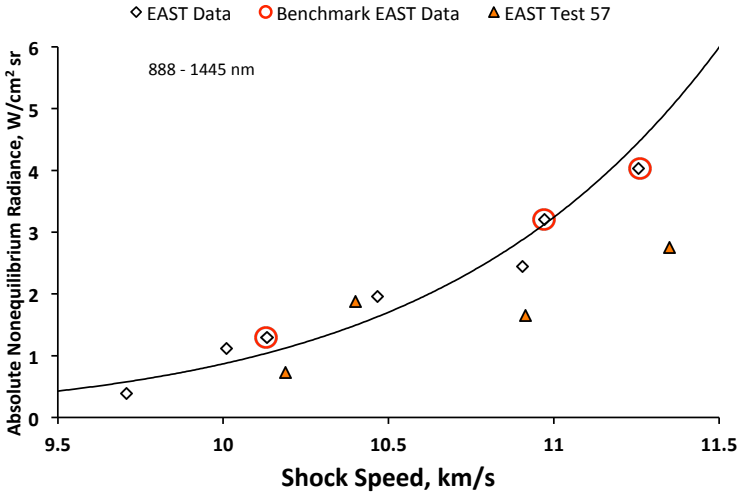

(c) Non-Equilibrium Metric at 0.1 Torr

Figure 15. IR EAST data.

References

[1]Cruden, B., Martinez, R., Grinstead, J., and Olejniczak, J., "Simultaneous Vacuum-Ultraviolet Through Near-IR Absolute Radiation Measurement with Spatiotemporal Resolution in An Electric Arc Shock Tube," *41st AIAA Thermophysics Conference*, San Antonio, Texas, 2009, AIAA-2009-4240.

[2]Cruden, B., "Absolute Radiation Measurements in Earth and Mars Entry Condition," *Radiation and Gas-Surface Interaction Phenomena in High-Speed Re-Entry*, Vol. Von Karman Institute Lecture Series, 2014.

[3]Cruden, B., "Electron Density Measurement in Re-entry Shocks for Lunar Return," *Journal of Thermophysics and Heat Transfer*, Vol. 26, 2012, pp. 222–230.

[4]Brandis, A., Johnston, C., Cruden, B., Prabhu, D., and Bose, D., "Uncertainty Analysis and Validation of Radiation Measurements for Earth Re-Entry," *Journal of Thermophysics and Heat Transfer*, Vol. 29, No. 2, 2015, pp. 209–221.

[5]Brandis, A., Johnston, C., Cruden, B., and Prabhu, D., "Equilibrium Radiative Heating from 9.5 to 15.5 km/s for Earth Atmospheric Entry," *Journal of Thermophysics and Heat Transfer*, Vol. xx, No. yy, 2016, Article in Advance, pp. 1–15.

[6]Brandis, A., Johnston, C., and Cruden, B., "Investigation of Non-equilibrium Radiation for Earth Re-Entry," *46th AIAA Thermophysics Conference*, Washington, D.C., 2016.

[7]Miki, K., Panesi, M., Prudencio, E., Maurente, A., Cheung, S., Jagodzinski, J., Goldstein, D., Prudhomme, S., Schulz, K., Simmons, C., Strand, J., and Varghese, P., "On The (In)Validation of a Thermochemical Model with EAST Shock Tube Radiation Measurements," *48th AIAA Aerospace Sciences Meeting*, Orlando, Florida, 2010, AIAA-2010-1557.

[8]Panesi, M., Babou, Y., and O., C., "Predictions of nonequilibrium radiation: analysis and comparison with EAST experiments," *40th Thermophysics Conference*, Seattle, Washington, 2008, AIAA-2008-3812.

[9]Lemal, A., Jacobs, C., Perrin, M., and Laux, C., "Prediction of Nonequilibrium Air Plasma Radiation Behind A Shock Wave," *Journal of Thermophysics and Heat Transfer*, Vol. 30, No. 1, 2016, pp. 197–210.

[10]Higdon, K., Goldstein, D., and Varghese, P., "Sensitivity Analysis of DSMC Parameters for Ionizing Hypersonic Flows," *45th AIAA Thermophysics Conference*, Dallas, TX, 2015, AIAA-2015-3371.

[11]Johnston, C., Brandis, A., and Bose, D., "Radiative Heating Uncertainty for Hyperbolic Earth Entry, Part 3: Comparisons with Electric Arc Shock-Tube Measurements," *Journal of Spacecraft and Rockets*, Vol. 50, No. 1, 2013, pp. 48–55.

[12]Johnston, C. O. and Kleb, B., "Uncertainty Analysis of Air Radiation for Lunar Return Shock Layers," *Journal of Spacecraft and Rockets*, Vol. 49, No. 3, 2012, pp. 425–434.

[13]Whiting, E., Park, C., Yen, L., Arnold, J., and Paterson, J., "NEQAIR96, Nonequilibrium and Equilibrium Radiative Transport and Spectra Program: User's Manual," Technical Report NASA RP-1389, Ames Research Center, Moffett Field, Moffett Field, 1996.

[14]Cruden, B. and Brandis, A., "Updates to the NEQAIR Radiation Solver," St. Andrews, Scotland, November 2014.

[15]Johnston, C., Hollis, B., and Sutton, K., "Spectrum Modeling for Air Shock-Layer Radiation at Lunar-Return Conditions," *Journal of Spacecraft and Rockets*, Vol. 45, No. 5, 2008, pp. 865–878.

[16]Johnston, C. O., Hollis, B., and Sutton, K., "Non-Boltzmann Modeling for Air Shock Layers at Lunar Return Conditions," *Journal of Spacecraft and Rockets*, Sep.-Oct. 2008.

[17]Brandis, A., Johnston, C., Cruden, B., and Prabhu, D., "Investigation of Nonequilibrium Radiation for Mars Entry," *51st AIAA Aerospace Sciences Meeting*, Grapevine, Texas, 2013, AIAA-2013-1055.

[18]Mazaheri, A., Gnoffo, P., Johnston, C., and Kleb, B., "LAURA Users Manual," Tech. Rep. NASA TM 2010-216836, 2010.

[19]Gnoffo, P., Gupta, R., and Shinn, J., "Conservation equations and physical models for hypersonic air flows in thermal and chemical nonequilibrium," Tech. Rep. NASA TP-2867, 1989.

[20]Wright, M., *A Family of Data-Parallel Relaxation Methods for the Navier-Stokes Equations*, Ph.D. thesis, University of Minnesota, 1997.

[21]Wright, M., Candler, G., and Bose, D., "Data-Parallel Line Relaxation Method for the Navier-Stokes Equations," *AIAA Journal*, Vol. 36, No. 9, 1998, pp. 1603–1609.

[22]Wright, M., White, T., and Mangini, N., "Data-Parallel Line Relaxation (DPLR) Code User Manual Acadia-Version 4.01.1," NASA/TM-2009-215388, NASA Ames Research Center, October 2009.

[23]Cruden, B., "Recent Progress in Entry Radiation Measurements in the NASA Ames Electric Arc Shock Tube Facility," *5th International Workshop on Radiation of High Temperature Gases in Atmospheric Entry*, Barcelona, Spain, October 2012.

[24]Brandis, A., Johnston, C., Cruden, B., Prabhu, D., Wray, A., Liu, Y., Schwenke, D., and Bose, D., "Validation of CO Fourth-Positive radiation for Mars Entry," *Journal of Quantitative Spectroscopy and Radiative Transfer*, Vol. 121, 2013, pp. 91–104.

A. Appendix - EAST Spectral Radiance

VUV: 0.1 Torr

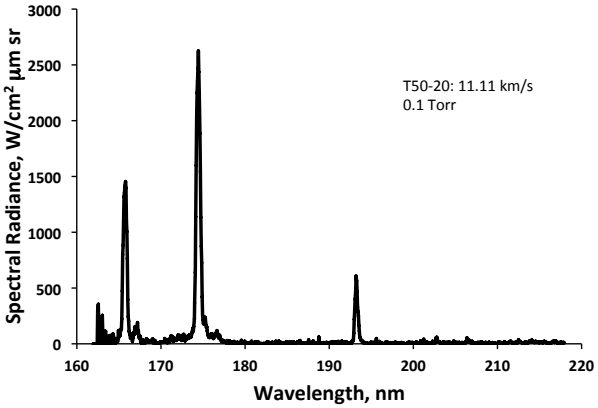

(a) Equilibrium

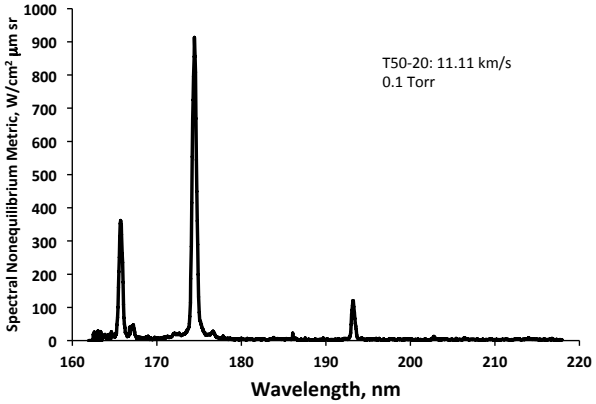

(b) Spectral Non-equilibrium Metric

Figure A1. T50-20: 11.11 km/s and 0.1 Torr.

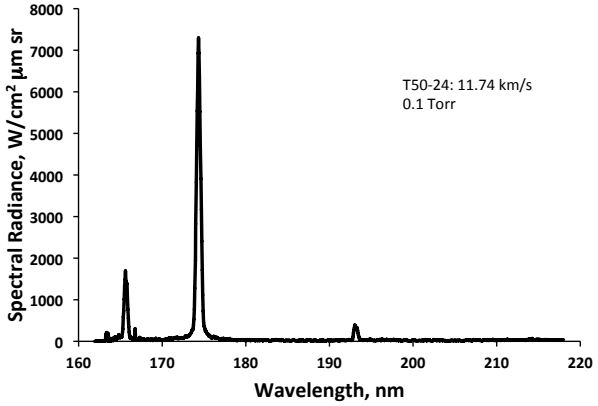

(a) Equilibrium

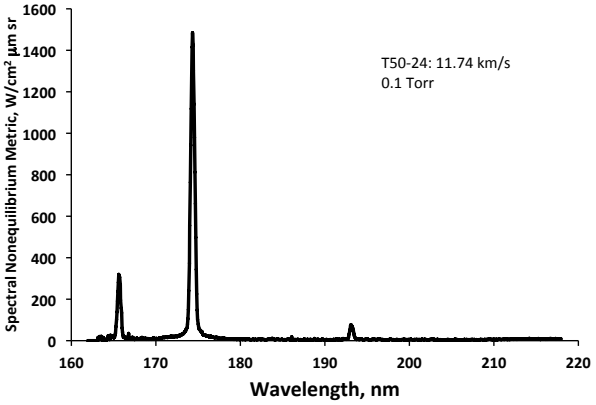

(b) Spectral Non-equilibrium Metric

Figure A2. T50-24: 11.74 km/s and 0.1 Torr.

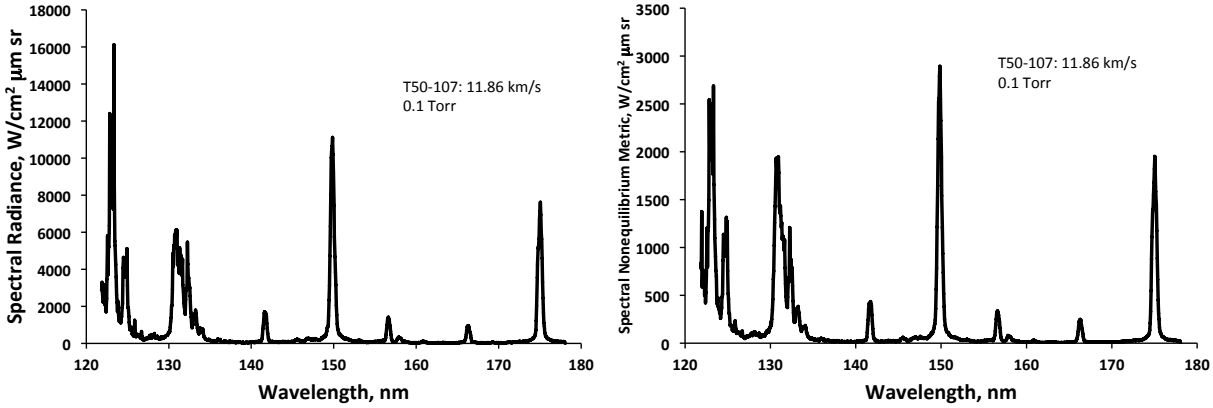

(a) Equilibrium (b) Spectral Non-equilibrium Metric

Figure A3. T50-107: 11.86 km/s and 0.1 Torr.

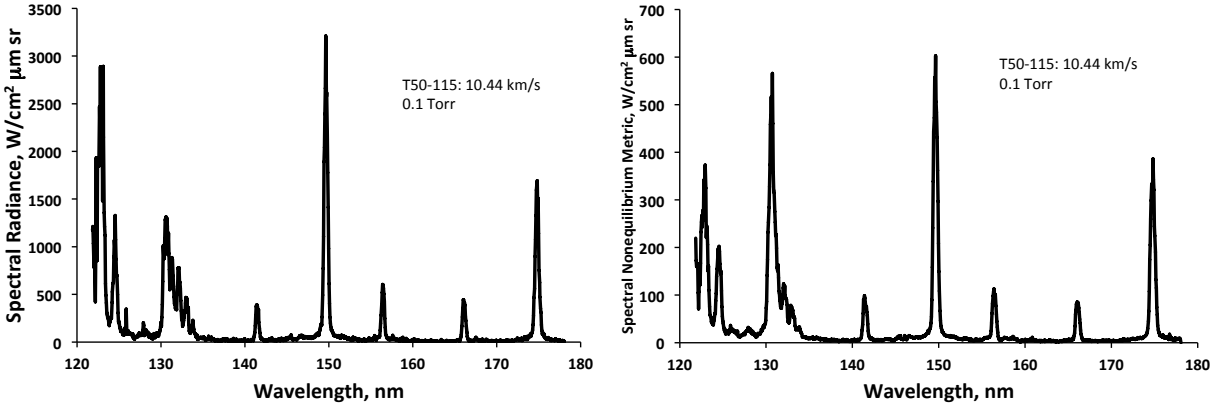

(a) Equilibrium (b) Spectral Non-equilibrium Metric

Figure A4. T50-115: 10.44 km/s and 0.1 Torr.

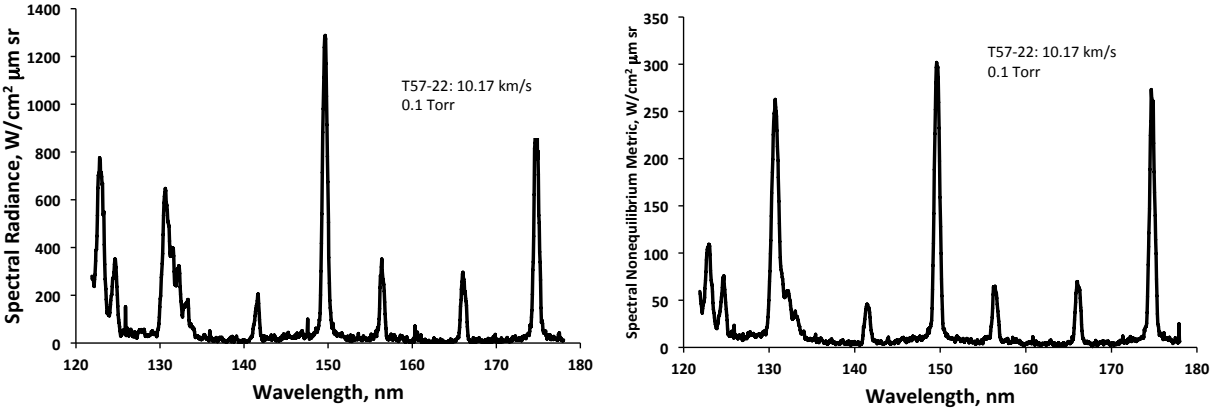

(a) Equilibrium (b) Spectral Non-equilibrium Metric

Figure A5. T57-22: 10.17 km/s and 0.1 Torr.

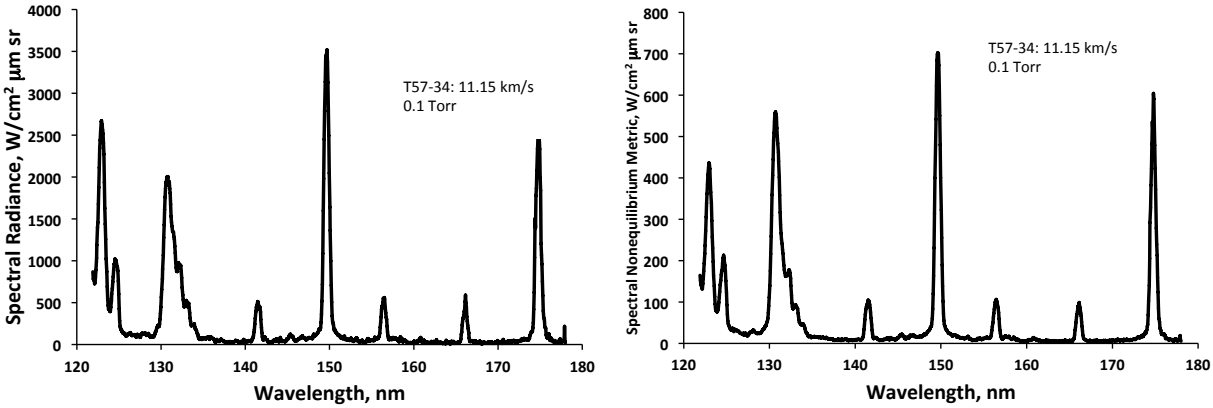

(a) Equilibrium (b) Spectral Non-equilibrium Metric

Figure A6. T57-34: 11.15 km/s and 0.1 Torr.

VUV: 0.2 Torr

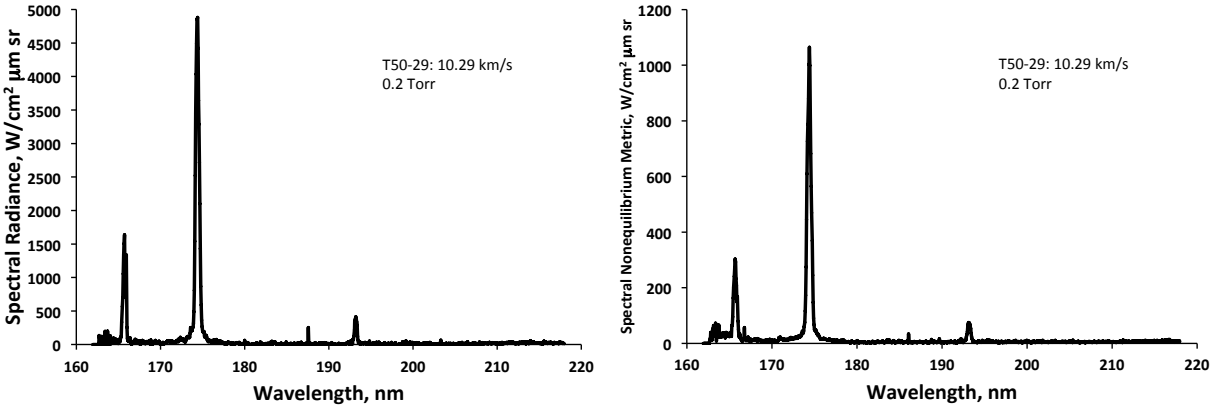

(a) Equilibrium (b) Spectral Non-equilibrium Metric

Figure A7. T50-29: 10.29 km/s and 0.2 Torr.

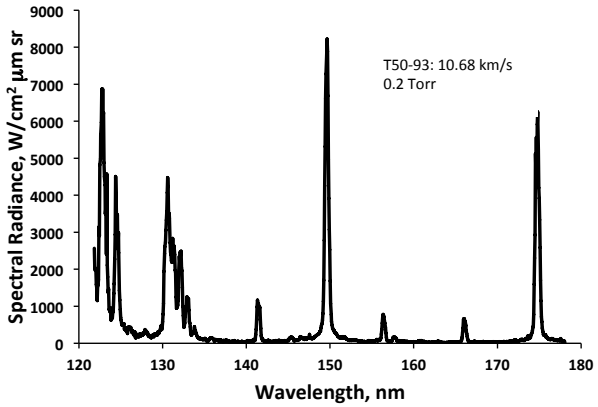

(a) Equilibrium

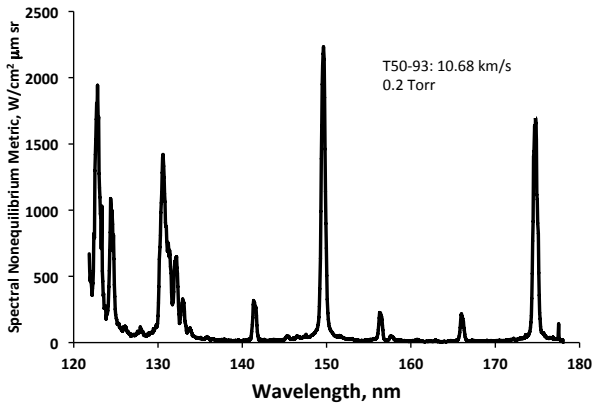

(b) Spectral Non-equilibrium Metric

Figure A8. T50-93: 10.68 km/s and 0.2 Torr.

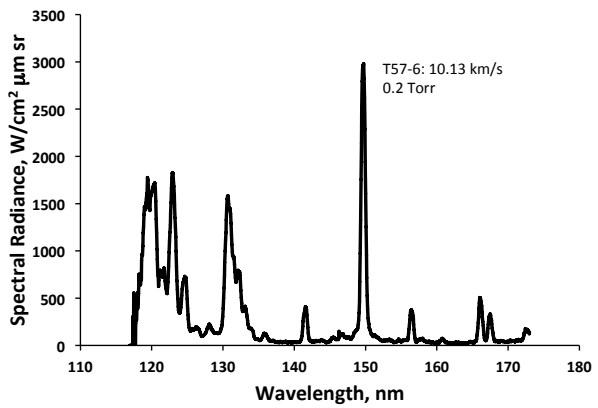

(a) Equilibrium

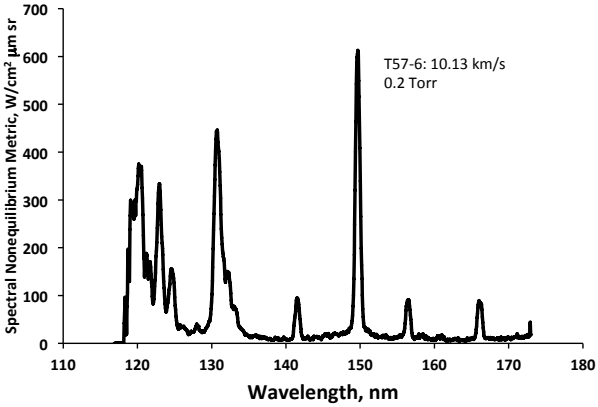

(b) Spectral Non-equilibrium Metric

Figure A9. T57-6: 10.13 km/s and 0.2 Torr.

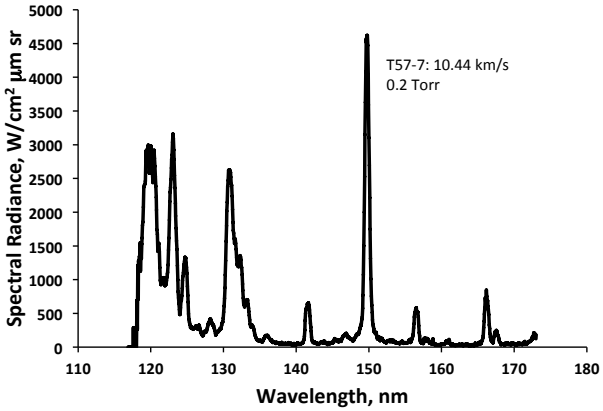

(a) Equilibrium

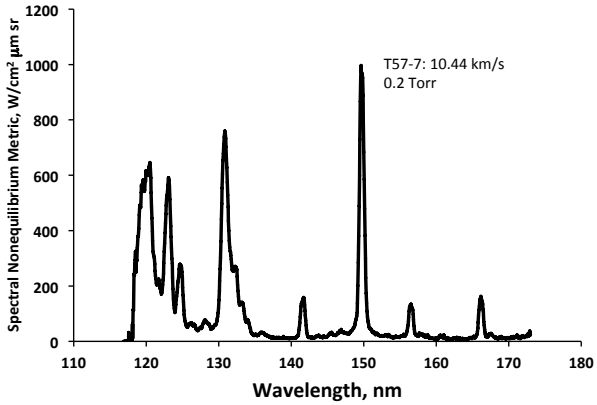

(b) Spectral Non-equilibrium Metric

Figure A10. T57-7: 10.44 km/s and 0.2 Torr.

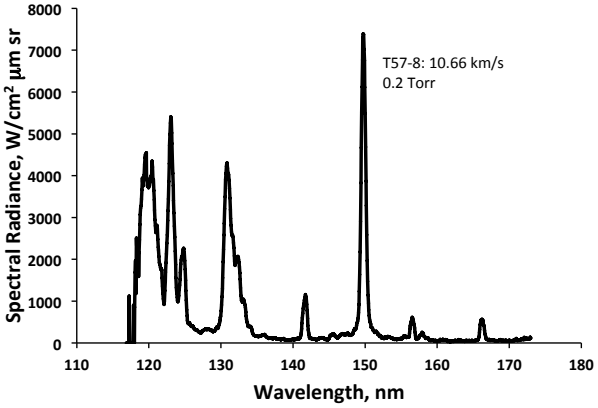

(a) Equilibrium

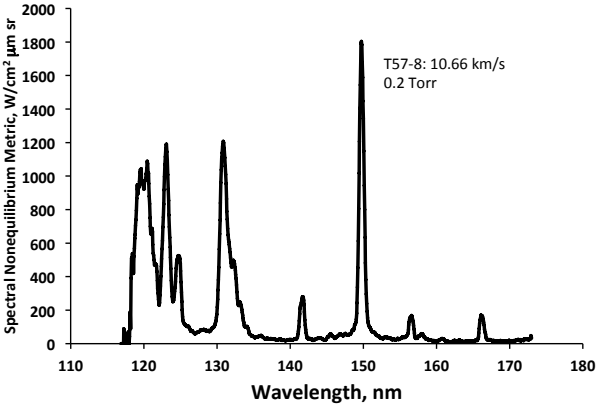

(b) Spectral Non-equilibrium Metric

Figure A11. T57-8: 10.66 km/s and 0.2 Torr.

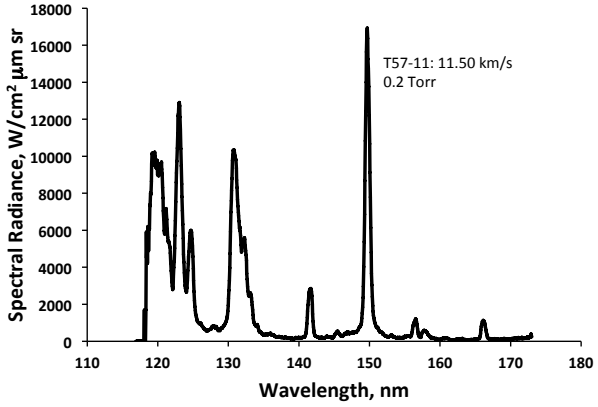

(a) Equilibrium

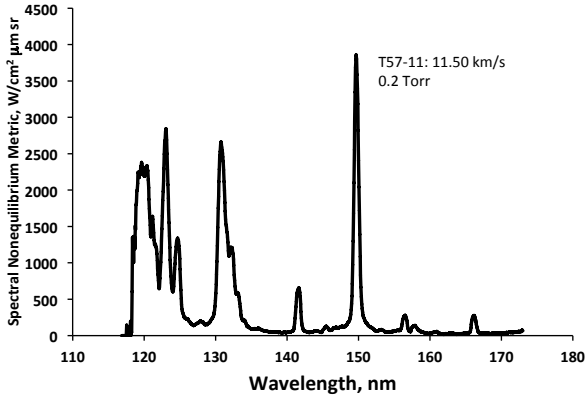

(b) Spectral Non-equilibrium Metric

Figure A12. T57-11: 11.5 km/s and 0.2 Torr.

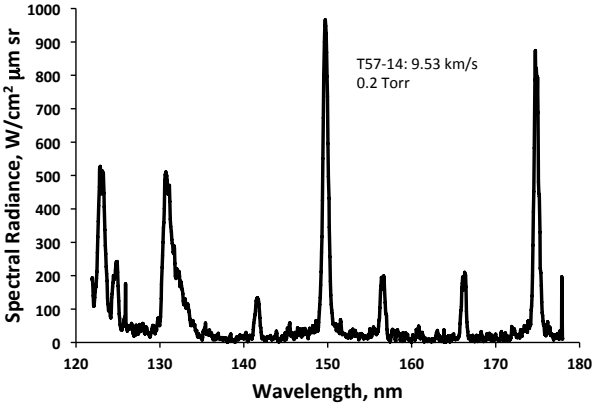

(a) Equilibrium

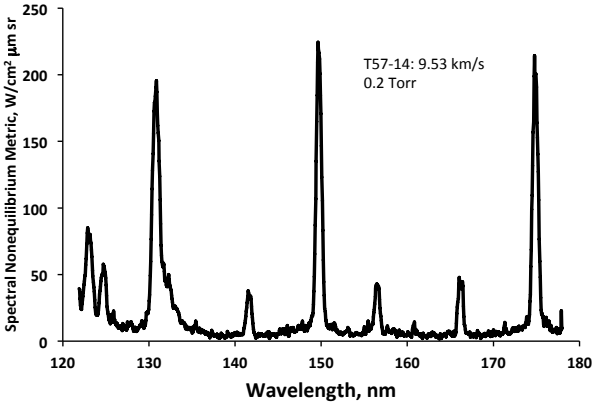

(b) Spectral Non-equilibrium Metric

Figure A13. T57-14: 9.53 km/s and 0.2 Torr.

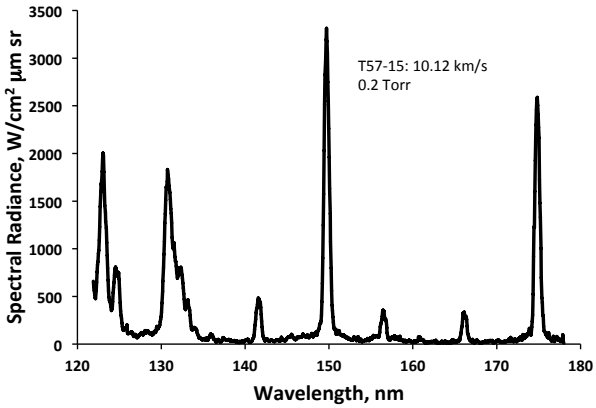

(a) Equilibrium

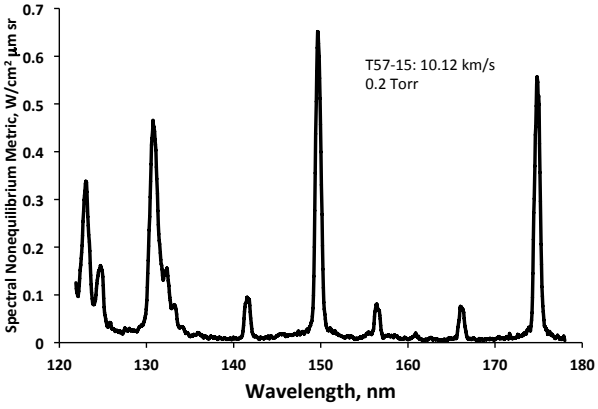

(b) Spectral Non-equilibrium Metric

Figure A14. T57-15: 10.12 km/s and 0.2 Torr.

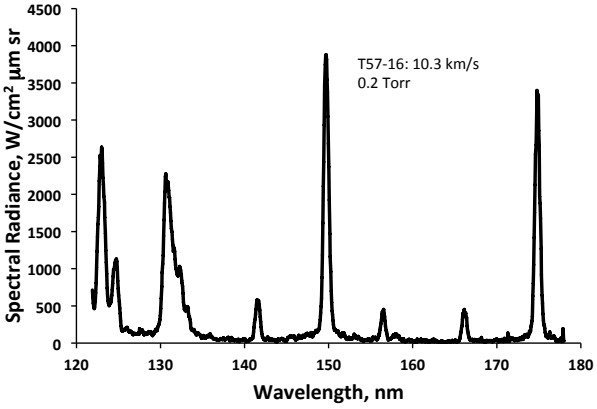

(a) Equilibrium

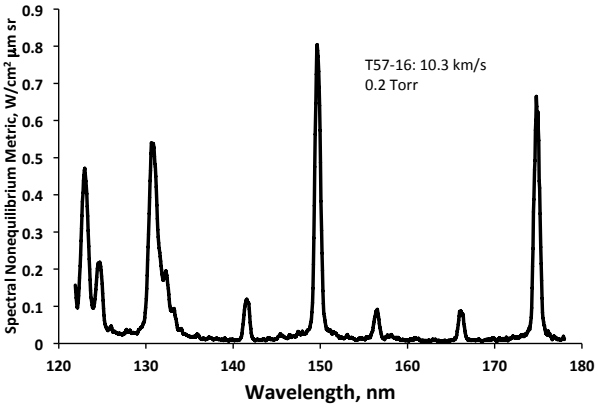

(b) Spectral Non-equilibrium Metric

Figure A15. T57-16: 10.3 km/s and 0.2 Torr.

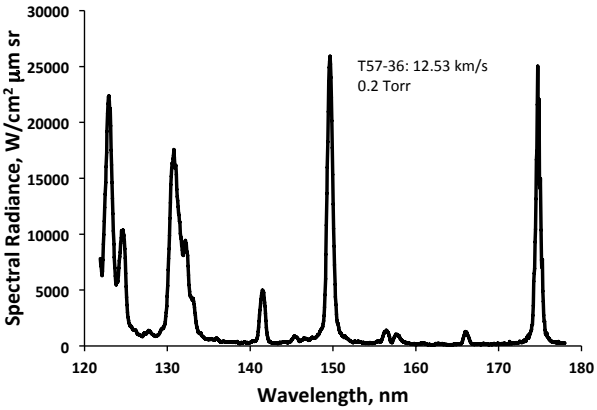

(a) Equilibrium

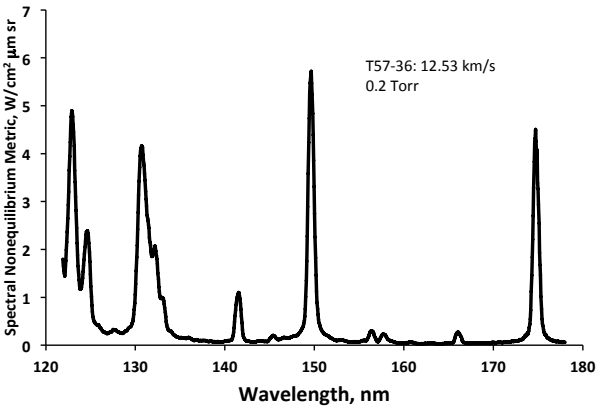

(b) Spectral Non-equilibrium Metric

Figure A16. T57-36: 12.53 km/s and 0.2 Torr.

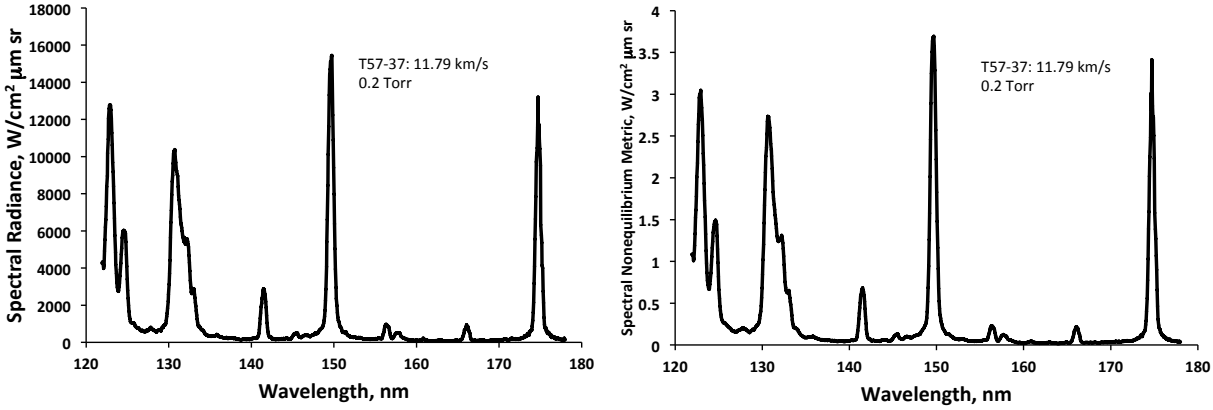

(a) Equilibrium (b) Spectral Non-equilibrium Metric

Figure A17. T57-37: 11.79 km/s and 0.2 Torr.

UV/Vis: 0.1 Torr

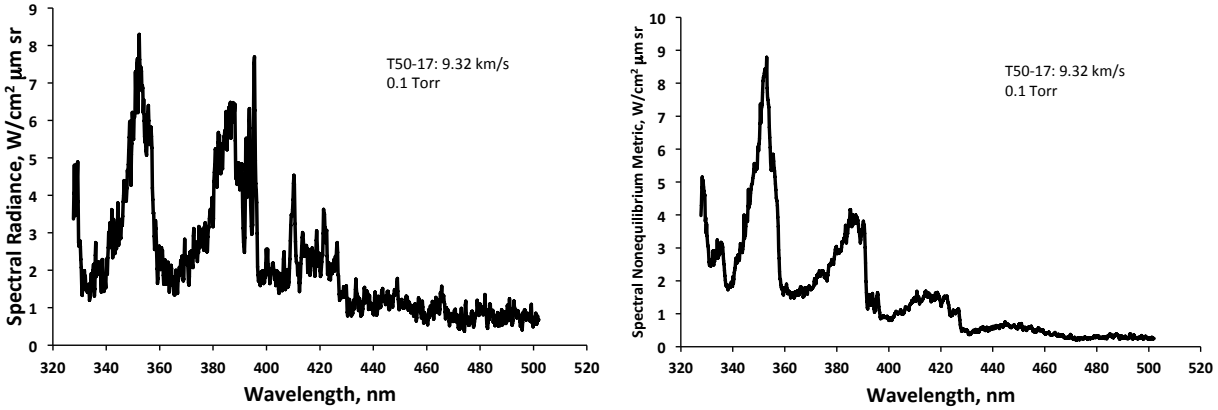

(a) Equilibrium (b) Spectral Non-equilibrium Metric

Figure A18. T50-17: 9.32 km/s and 0.1 Torr.

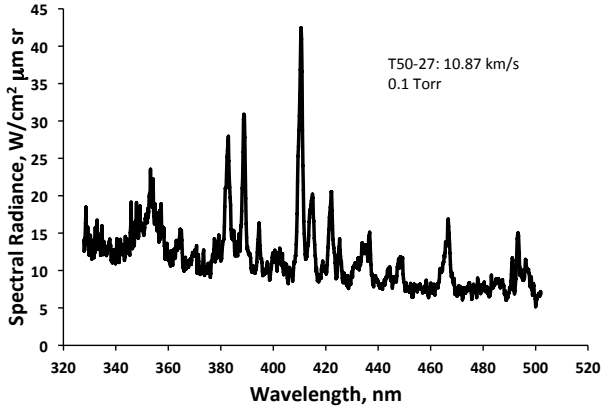

(a) Equilibrium

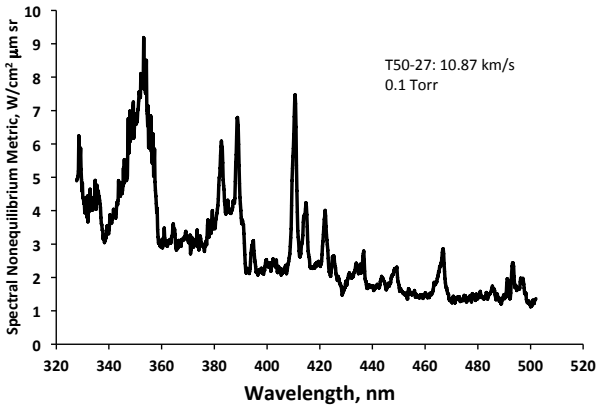

(b) Spectral Non-equilibrium Metric

Figure A19. T50-27: 10.87 km/s and 0.1 Torr.

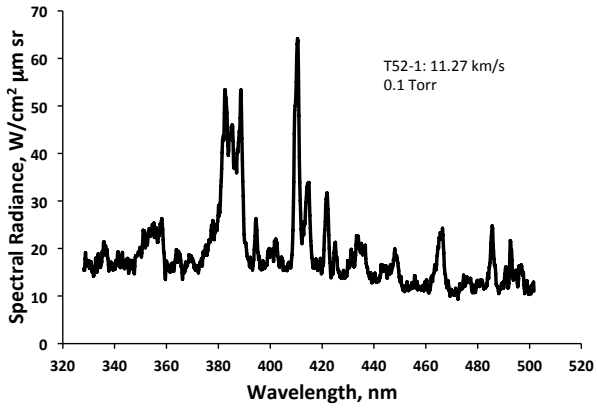

(a) Equilibrium

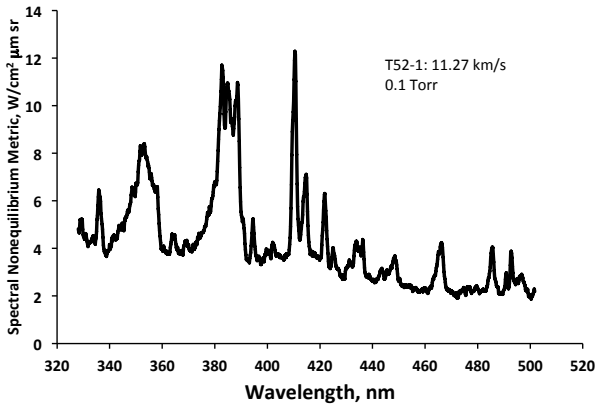

(b) Spectral Non-equilibrium Metric

Figure A20. T52-1: 11.27 km/s and 0.1 Torr.

UV/Vis: 0.2 Torr

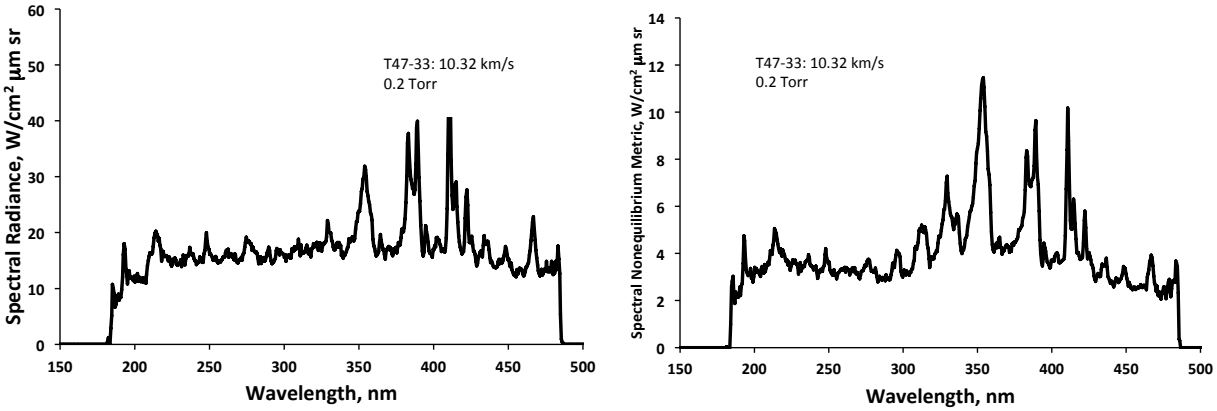

(a) Equilibrium (b) Spectral Non-equilibrium Metric

Figure A21. T47-33: 10.32 km/s and 0.2 Torr.

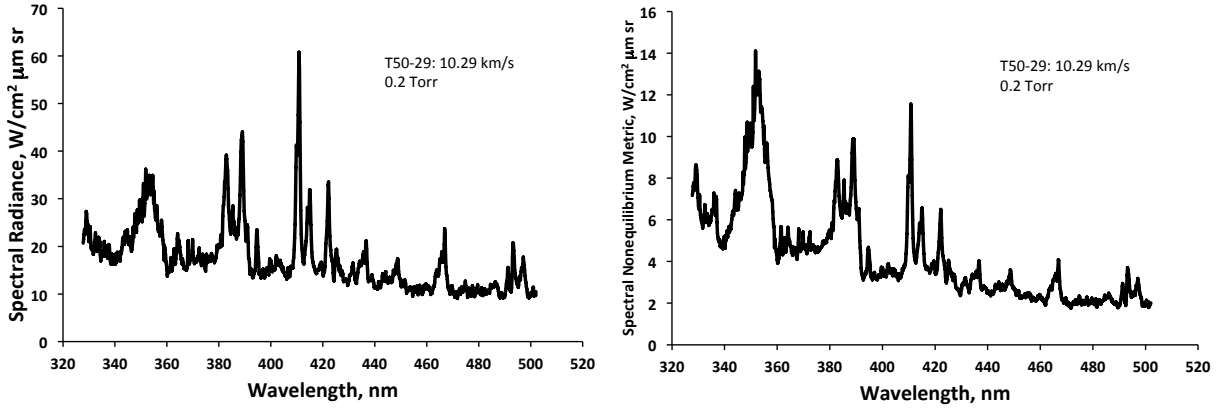

(a) Equilibrium (b) Spectral Non-equilibrium Metric

Figure A22. T50-29: 10.29 km/s and 0.2 Torr.

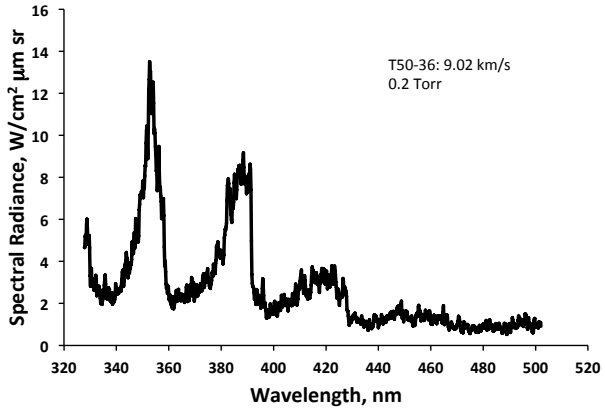

(a) Equilibrium

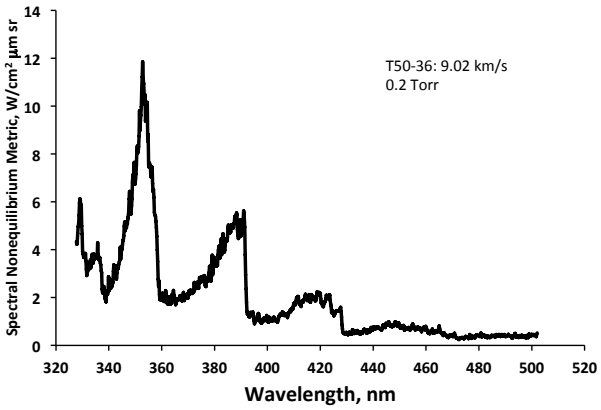

(b) Spectral Non-equilibrium Metric

Figure A23. T50-36: 10.36 km/s and 0.2 Torr.

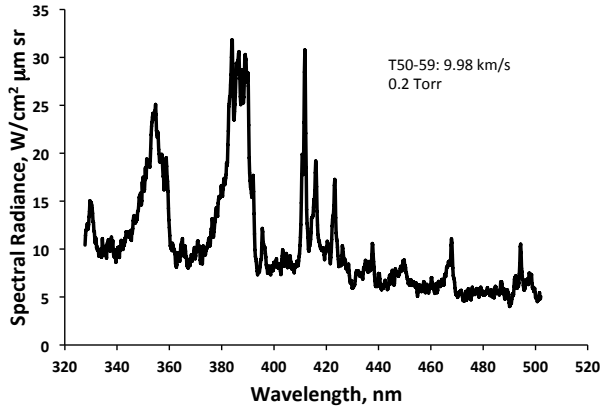

(a) Equilibrium

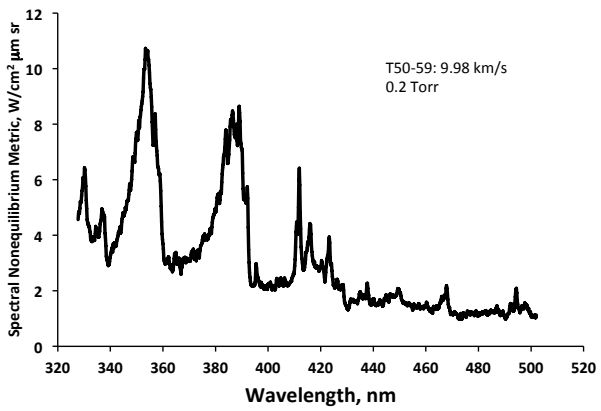

(b) Spectral Non-equilibrium Metric

Figure A24. T50-59: 10.36 km/s and 0.2 Torr.

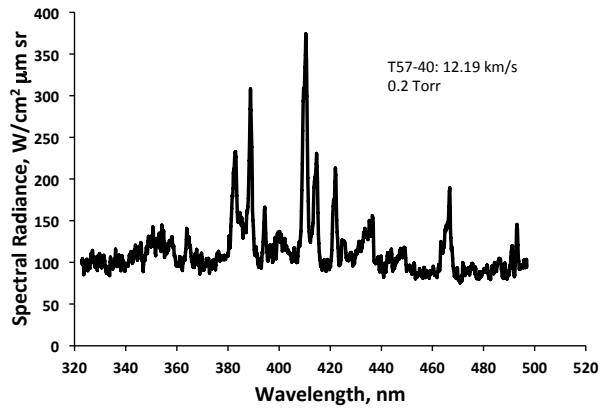

(a) Equilibrium

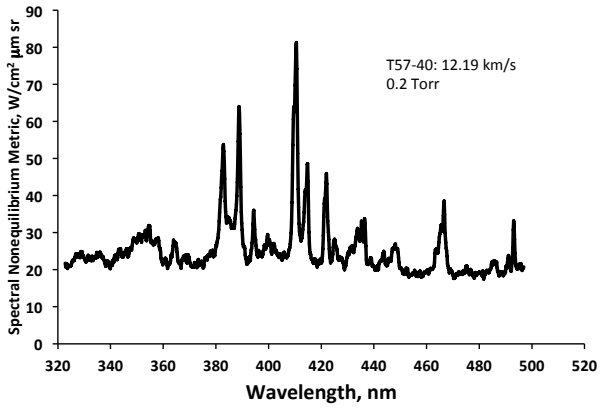

(b) Spectral Non-equilibrium Metric

Figure A25. T57-40: 10.36 km/s and 0.2 Torr.

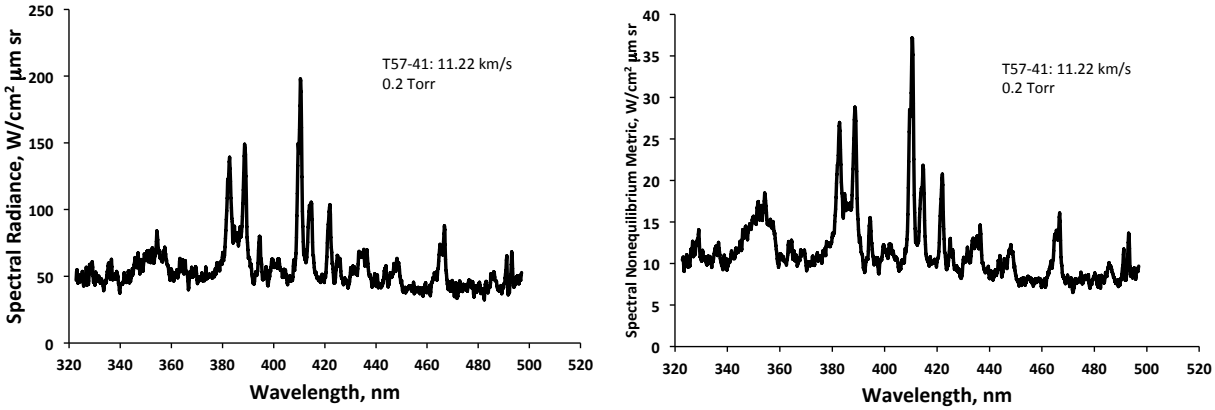

(a) Equilibrium (b) Spectral Non-equilibrium Metric

Figure A26. T57-41: 10.36 km/s and 0.2 Torr.

Vis/NIR: 0.1 Torr

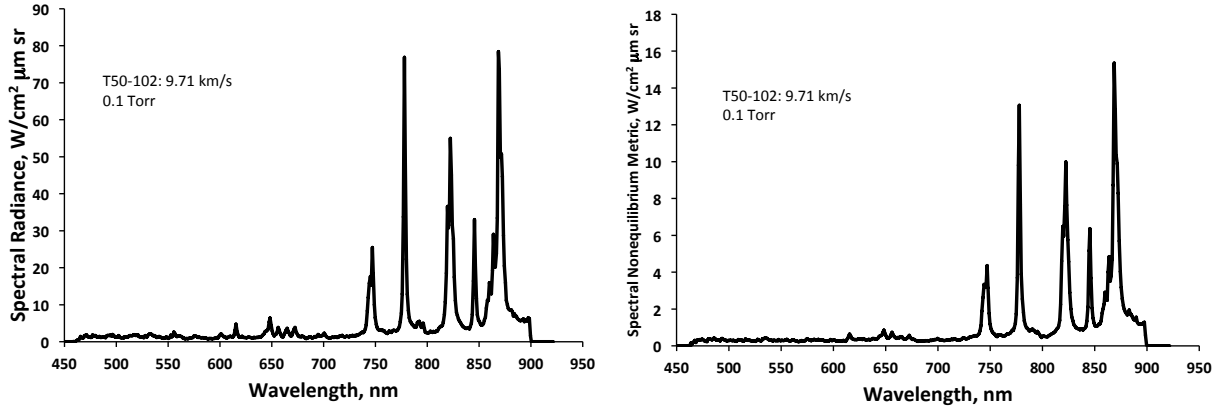

(a) Equilibrium (b) Spectral Non-equilibrium Metric

Figure A27. T50-102: 9.71 km/s and 0.1 Torr.

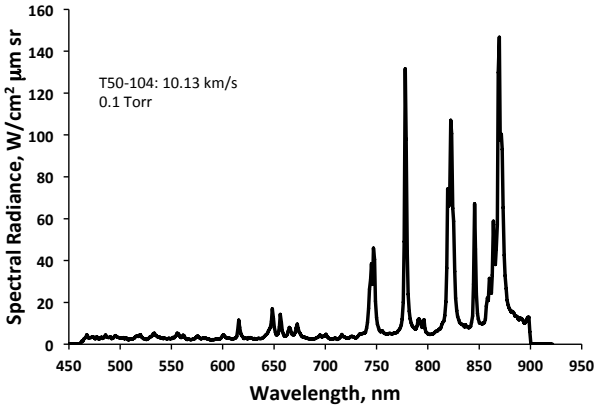

(a) Equilibrium

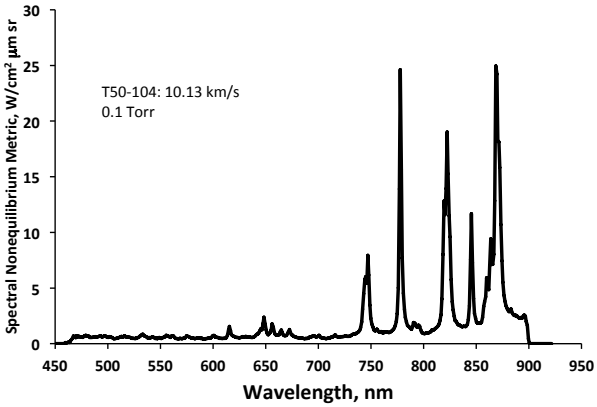

(b) Spectral Non-equilibrium Metric

Figure A28. T50-104: 10.13 km/s and 0.1 Torr.

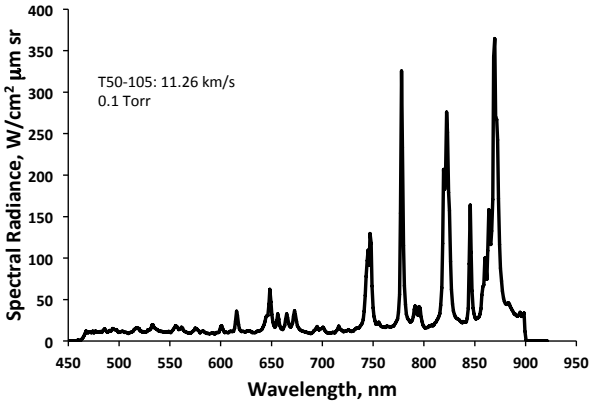

(a) Equilibrium

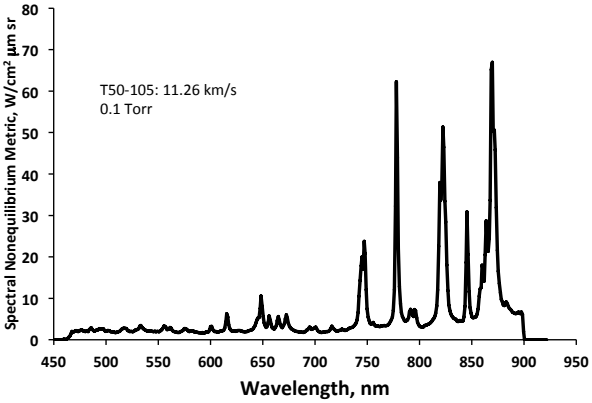

(b) Spectral Non-equilibrium Metric

Figure A29. T50-105: 11.26 km/s and 0.1 Torr.

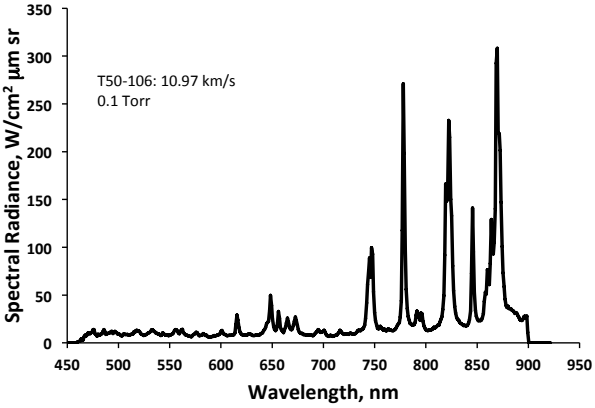

(a) Equilibrium

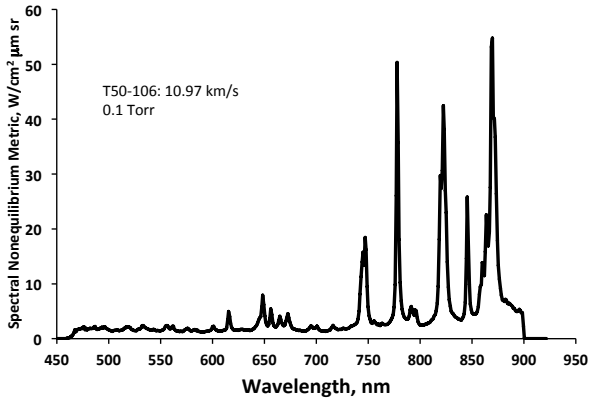

(b) Spectral Non-equilibrium Metric

Figure A30. T50-106: 10.97 km/s and 0.1 Torr.

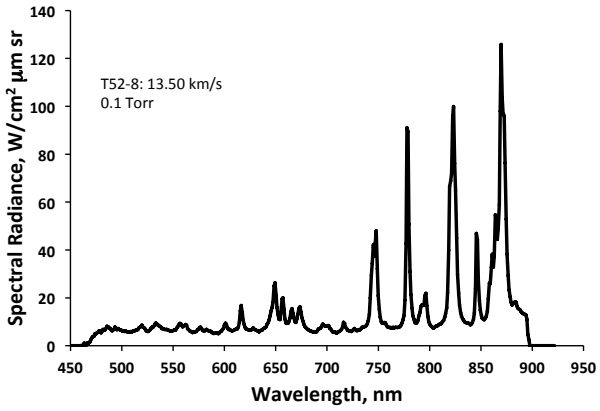

(a) Equilibrium

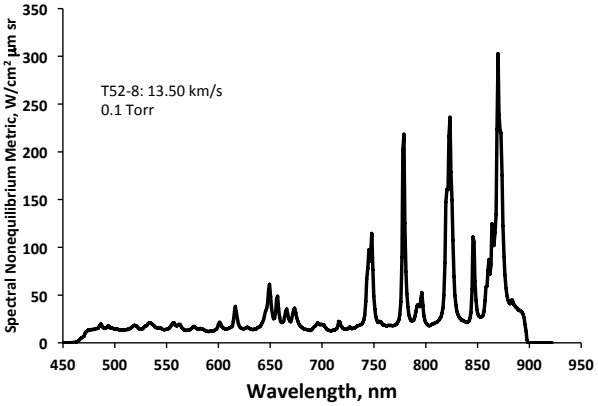

(b) Spectral Non-equilibrium Metric

Figure A31. T52-8: 13.50 km/s and 0.1 Torr.

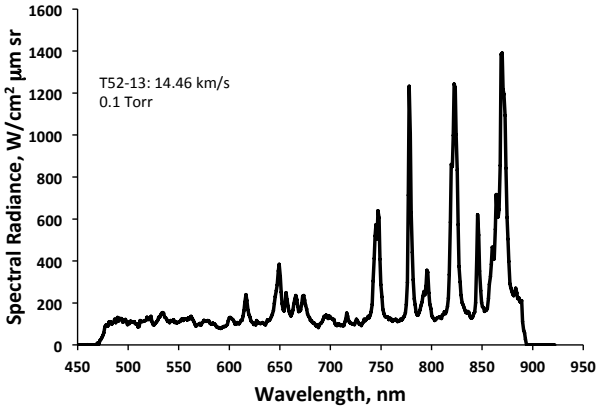

(a) Equilibrium

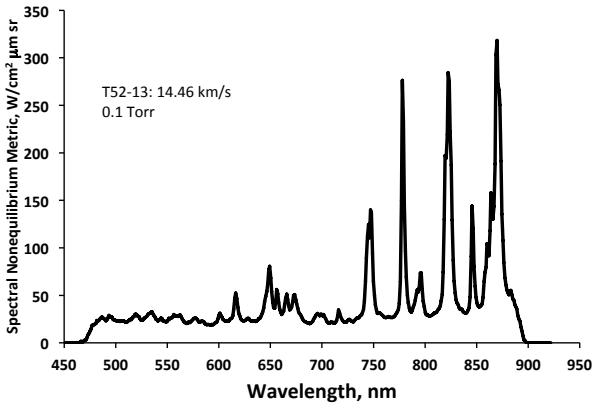

(b) Spectral Non-equilibrium Metric

Figure A32. T52-13: 14.46 km/s and 0.1 Torr.

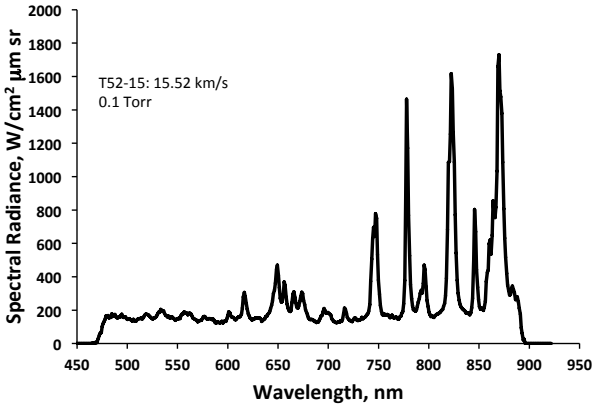

(a) Equilibrium

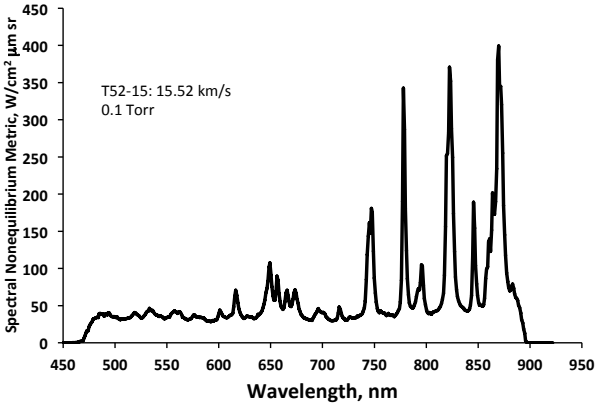

(b) Spectral Non-equilibrium Metric

Figure A33. T52-15: 15.52 km/s and 0.1 Torr.

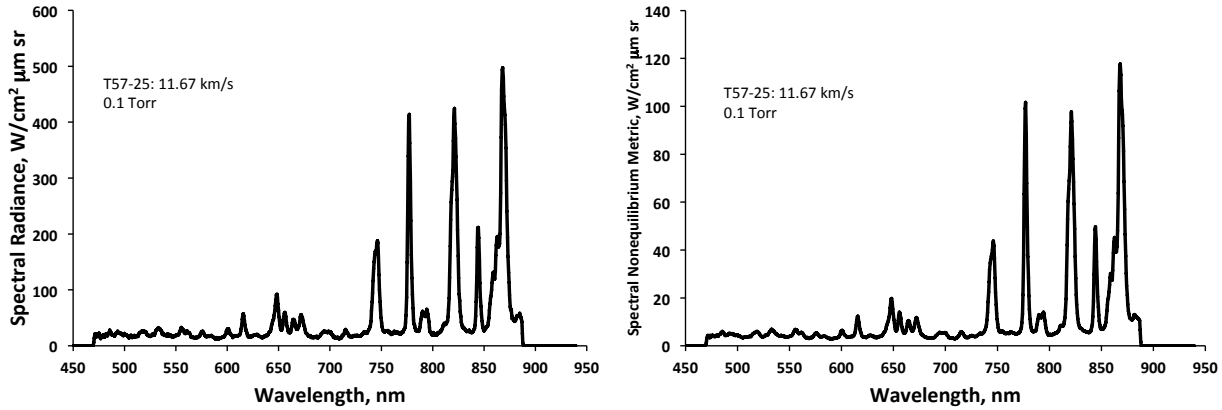

(a) Equilibrium (b) Spectral Non-equilibrium Metric

Figure A34. T57-25: 11.67 km/s and 0.1 Torr.

Vis/NIR: 0.2 Torr

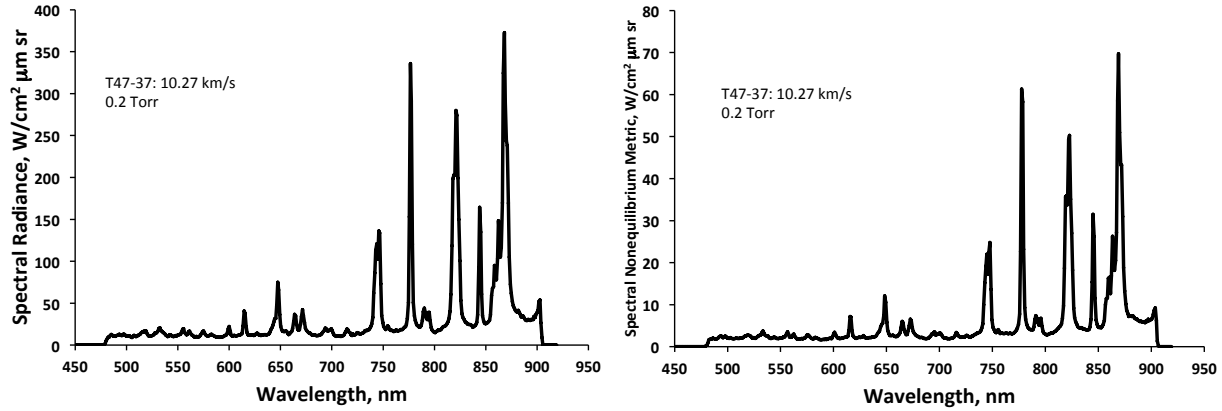

(a) Equilibrium (b) Spectral Non-equilibrium Metric

Figure A35. T47-37: 10.27 km/s and 0.2 Torr.

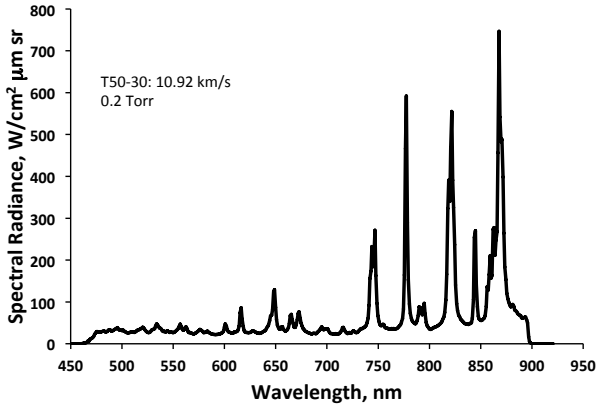

(a) Equilibrium

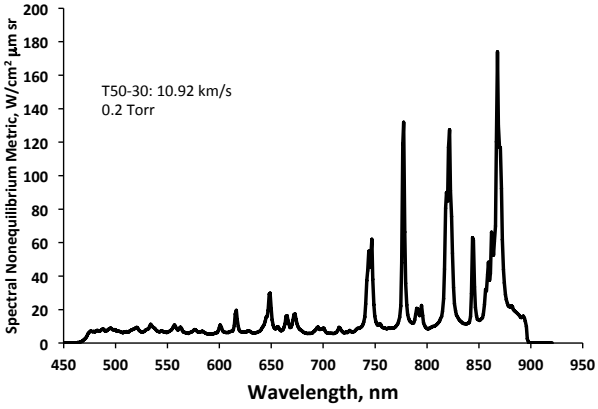

(b) Spectral Non-equilibrium Metric

Figure A36. T50-30: 10.92 km/s and 0.2 Torr.

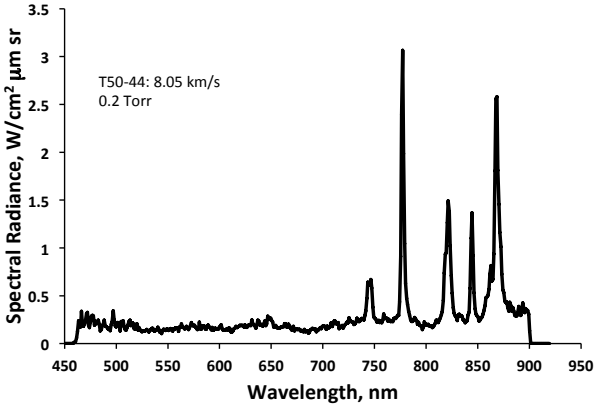

(a) Equilibrium

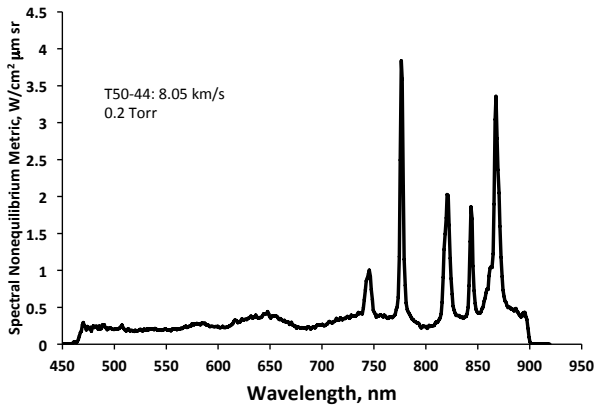

(b) Spectral Non-equilibrium Metric

Figure A37. T50-44: 8.05 km/s and 0.2 Torr.

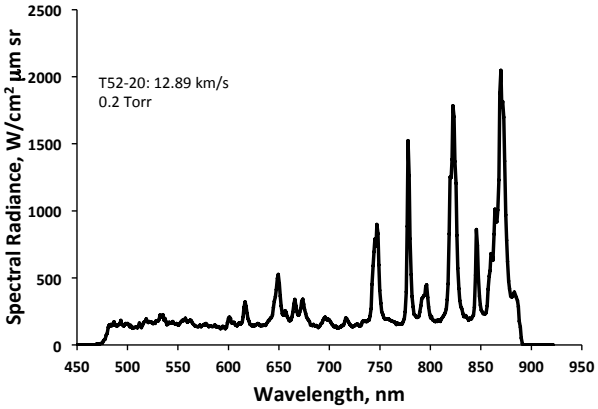

(a) Equilibrium

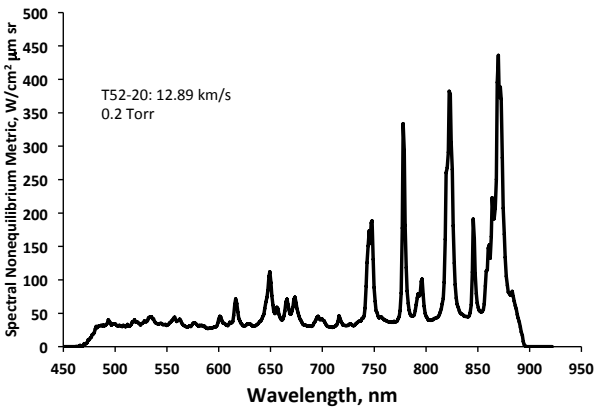

(b) Spectral Non-equilibrium Metric

Figure A38. T52-20: 12.89 km/s and 0.2 Torr.

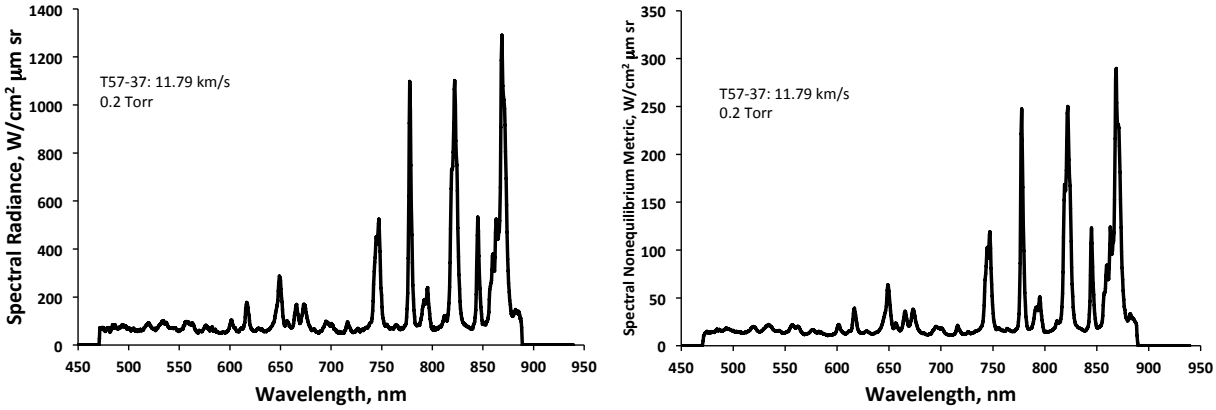

(a) Equilibrium (b) Spectral Non-equilibrium Metric

Figure A39. T57-37: 11.79 km/s and 0.2 Torr.

IR: 0.1 Torr

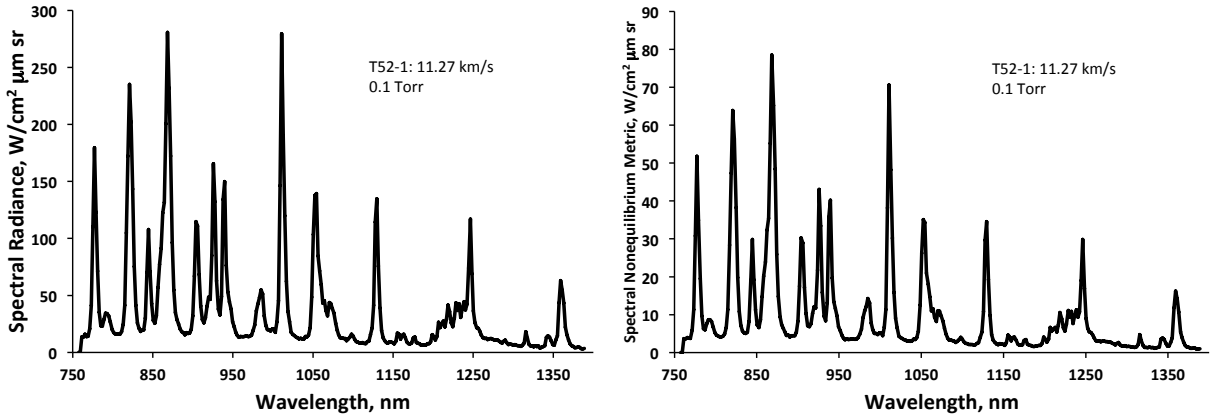

(a) Equilibrium (b) Spectral Non-equilibrium Metric

Figure A40. T52-1: 11.27 km/s and 0.1 Torr.

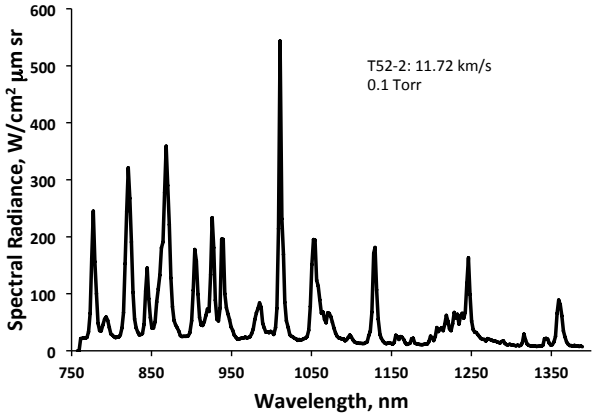

(a) Equilibrium

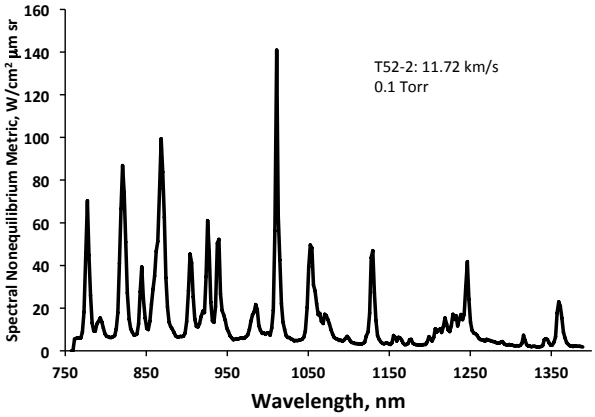

(b) Spectral Non-equilibrium Metric

Figure A41. T52-2: 11.72 km/s and 0.1 Torr.

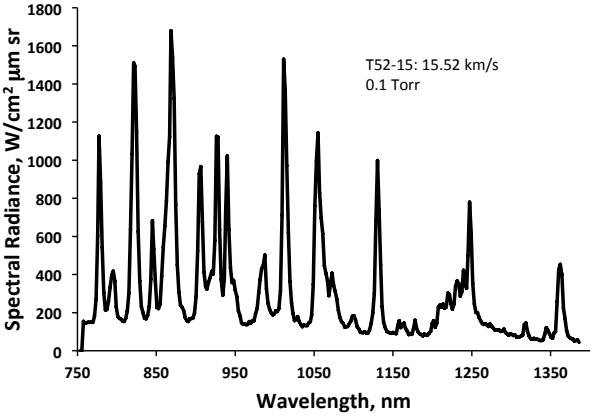

(a) Equilibrium

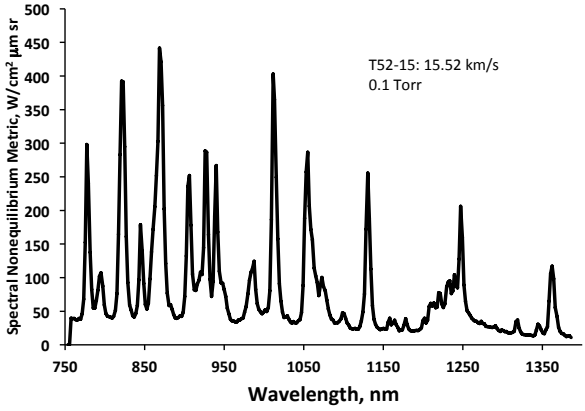

(b) Spectral Non-equilibrium Metric

Figure A42. T52-15: 15.52 km/s and 0.1 Torr.

IR: 0.2 Torr

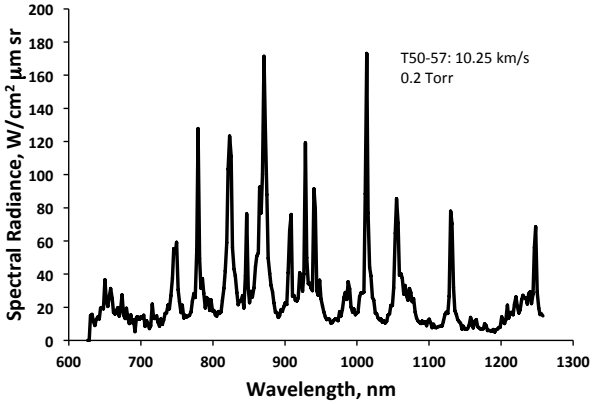

(a) Equilibrium

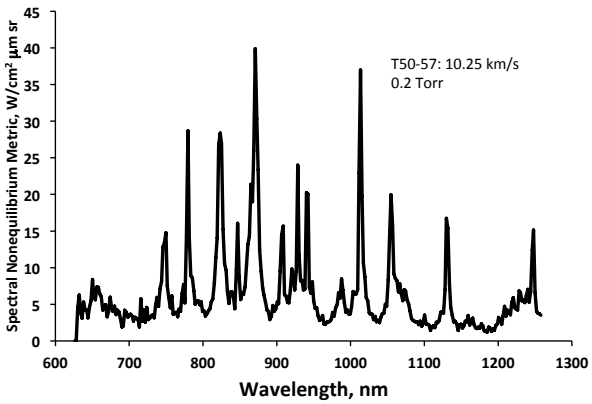

(b) Spectral Non-equilibrium Metric

Figure A43. T50-57: 10.25 km/s and 0.2 Torr.

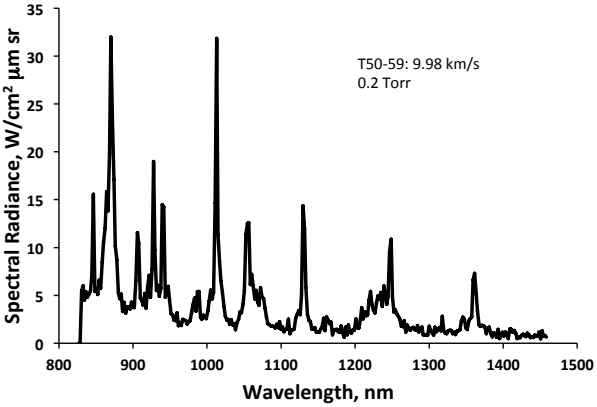

(a) Equilibrium

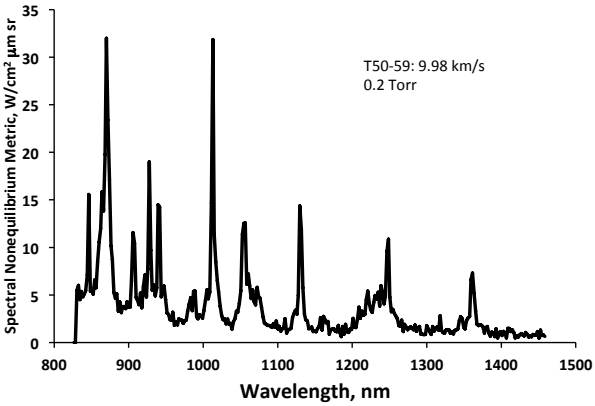

(b) Spectral Non-equilibrium Metric

Figure A44. T50-59: 9.98 km/s and 0.2 Torr.

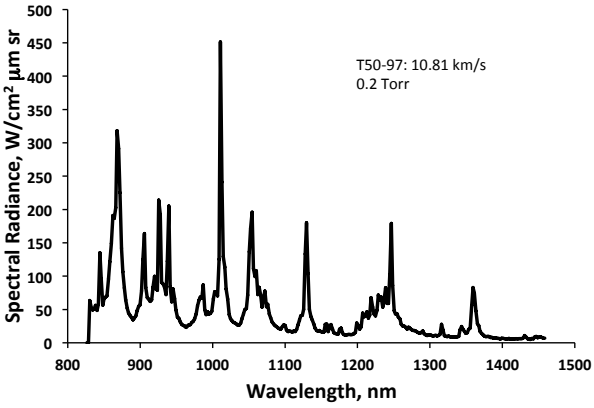

(a) Equilibrium

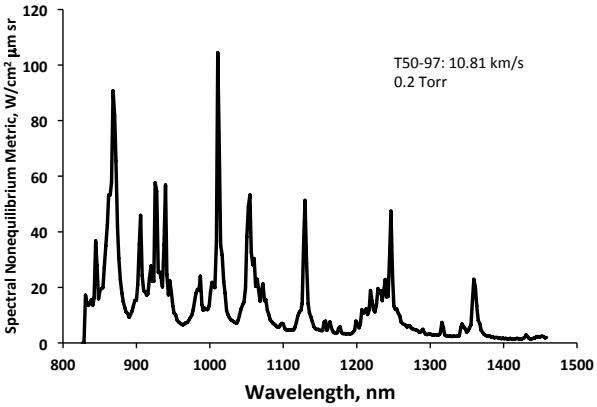

(b) Spectral Non-equilibrium Metric

Figure A45. T50-97: 10.81 km/s and 0.2 Torr.

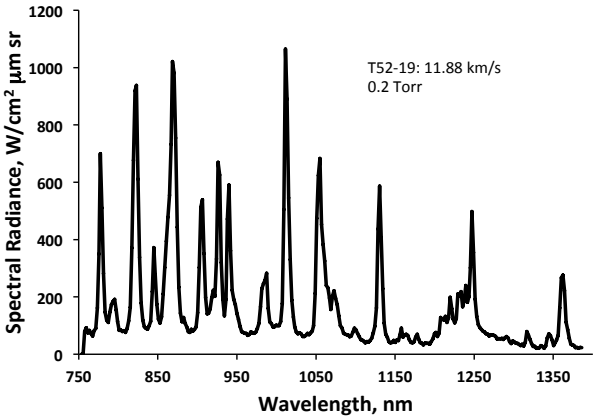

(a) Equilibrium

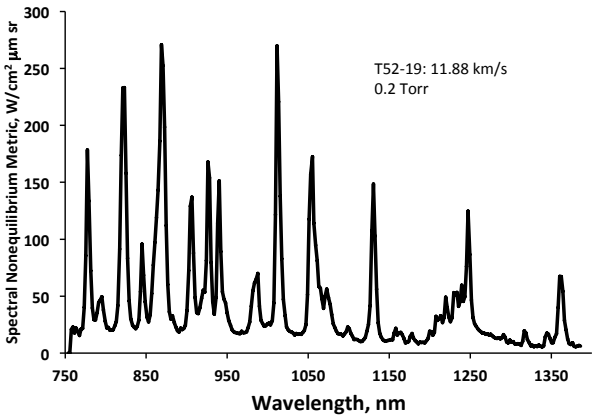

(b) Spectral Non-equilibrium Metric

Figure A46. T52-19: 11.88 km/s and 0.2 Torr.

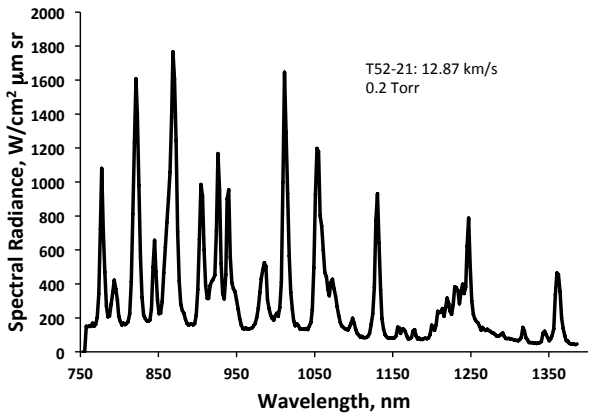

(a) Equilibrium

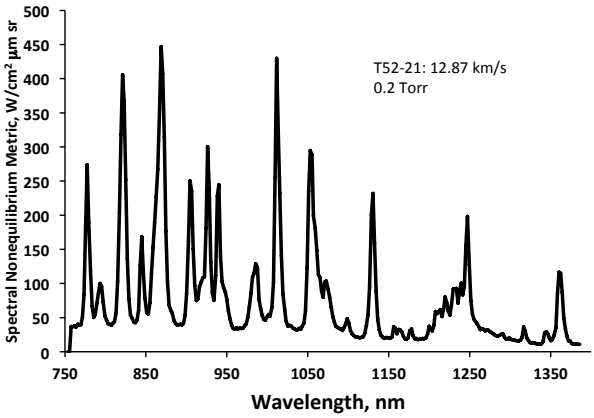

(b) Spectral Non-equilibrium Metric

Figure A47. T52-21: 11.88 km/s and 0.2 Torr.

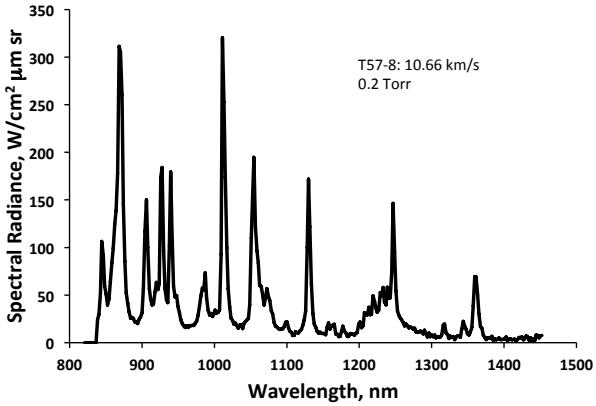

(a) Equilibrium

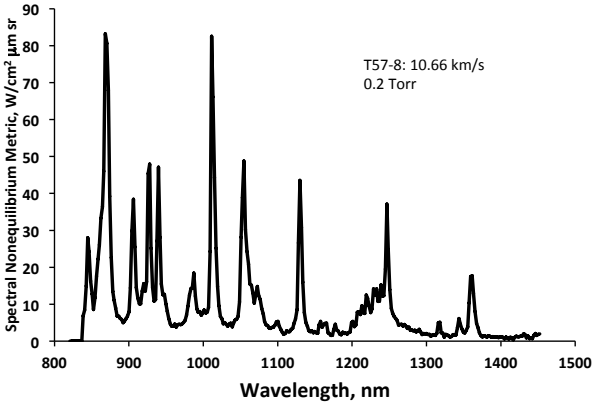

(b) Spectral Non-equilibrium Metric

Figure A48. T57-8: 10.66 km/s and 0.2 Torr.

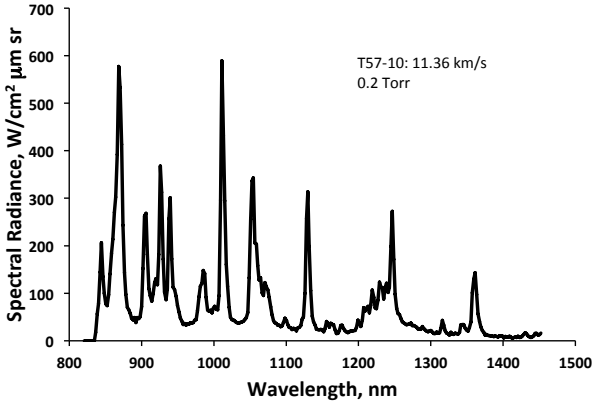

(a) Equilibrium

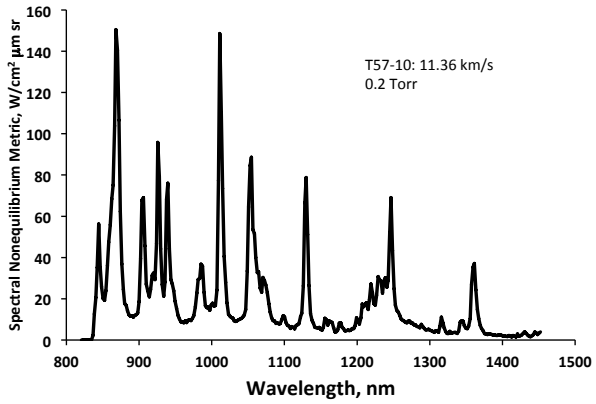

(b) Spectral Non-equilibrium Metric

Figure A49. T57-10: 11.36 km/s and 0.2 Torr.

B. Appendix - Shock Time of Arrival Data

The shock time of arrival data obtained with PCB's for all of the benchmark EAST datasets is presented in Tables B1 to B4.

Table B1. Tests 47 and 50 (Part I) EAST Shock Time of Arrivals

Distance, cm	Time, μs										
	T47-33	T47-37	T50-17	T50-20	T50-24	T50-27	T50-29	T50-30	T50-36	T50-44	T50-57
106.045	N/A	N/A	168.32	150.39	163.97	167.02	164.77	157.89	N/A	N/A	151.90
220.345	N/A	N/A	263.28	246.60	290.47	295.34	289.32	277.24	N/A	N/A	239.79
374.80748	311.79	311.01	398.10	420.80	509.90	516.60	N/A	N/A	395.13	435.05	363.86
496.72748	415.27	413.14	510.26	512.60	626.50	637.93	621.74	591.52	510.47	561.63	465.76
618.64748	524.21	520.02	N/A	N/A	740.90	N/A	N/A	N/A	N/A	N/A	N/A
699.92748	599.51	594.59	709.78	672.15	818.60	838.53	817.62	774.41	716.09	790.14	647.02
710.08748	609.04	604.07	720.44	680.70	828.40	848.88	827.28	783.40	N/A	N/A	656.54
756.6025	653.19	648.10	768.50	721.58	872.61	893.63	871.64	825.35	N/A	858.16	700.79
764.8575	660.95	655.98	777.18	728.88	880.50	901.23	879.52	832.84	785.83	N/A	708.73
773.1125	668.78	663.81	785.92	736.31	887.82	908.75	887.53	N/A	N/A	878.54	716.77
776.2875	672.02	667.12	789.36	739.22	890.61	911.74	890.64	843.26	798.55	882.46	719.85
779.4625	675.08	670.20	793.14	742.07	893.45	914.70	893.72	846.21	802.07	886.58	723.06
782.6375	678.07	673.29	N/A	744.99	896.01	917.51	896.70	848.99	805.58	890.39	726.07
785.8125	681.23	676.40	799.94	747.92	898.98	920.60	899.91	852.09	809.22	894.59	729.20
788.9875	684.11	679.36	802.84	750.68	901.56	923.36	902.89	854.93	812.49	898.14	732.23
792.1625	687.36	682.60	806.60	753.60	904.30	926.30	906.02	857.92	816.10	N/A	735.35
795.3375	690.36	685.63	810.06	756.50	907.06	929.25	909.13	860.82	819.70	906.23	738.61
798.5125	693.54	N/A	813.30	759.19	909.60	932.00	911.96	863.56	822.99	910.07	741.52

Table B2. Test 50 (Part II) EAST Shock Time of Arrivals

Distance, cm	Time, μs									
	T50-59	T50-93	T50-97	T50-102	T50-103	T50-104	T50-105	T50-106	T50-107	T50-115
	T50-59	T50-93	T50-97	T50-102	T50-103	T50-104	T50-105	T50-106	T50-107	T50-115
106.045	151.99	144.22	143.11	167.10	173.83	167.38	156.50	164.21	179.51	158.95
220.345	241.38	N/A	N/A	294.34	313.62	302.05	280.62	294.54	316.15	281.12
374.80748	367.78	N/A	N/A	518.70	545.30	518.50	N/A	N/A	N/A	N/A
496.72748	473.05	N/A	N/A	N/A	N/A	N/A	N/A	N/A	N/A	597.89
618.64748	N/A	554.28	549.28	756.86	789.99	746.77	683.03	707.66	712.32	N/A
699.92748	660.62	626.46	620.64	N/A	N/A	N/A	N/A	N/A	N/A	780.34
710.08748	670.41	635.73	629.81	847.56	875.73	833.83	763.26	789.47	787.24	789.82
756.6025	716.11	678.42	672.08	894.20	919.47	879.12	804.67	831.44	825.84	833.39
764.8575	724.36	N/A	679.73	902.89	927.25	887.17	811.90	838.88	832.70	N/A
773.1125	732.68	693.84	687.34	911.43	935.13	895.34	819.23	846.32	839.66	849.08
776.2875	735.83	696.80	690.28	914.63	938.09	898.39	822.01	849.26	842.32	851.50
779.4625	739.16	699.85	693.28	918.04	941.09	901.66	824.66	852.14	845.08	855.28
782.6375	742.22	702.39	696.09	921.23	944.21	904.69	827.72	855.09	847.75	858.19
785.8125	745.47	705.75	699.08	924.70	947.35	907.96	830.51	858.12	850.47	861.07
788.9875	748.60	708.61	701.95	927.63	950.16	910.79	833.28	860.79	853.05	864.15
792.1625	751.83	711.63	704.85	0.00	953.27	914.05	835.99	863.13	855.72	867.37
795.3375	754.97	714.66	707.94	934.27	956.20	917.22	838.92	866.59	858.40	870.26
798.5125	758.09	717.66	710.87	937.56	959.33	920.34	841.78	869.50	861.11	873.43

Table B3. Test 52 EAST Shock Time of Arrivals

Distance, cm	Time, μs									
	T52-1	T52-2	T52-5	T52-7	T52-8	T52-13	T52-15	T52-19	T52-20	T52-21
106.045	177.73	155.14	148.81	139.91	154.91	146.93	143.92	151.94	134.65	130.08
220.345	300.72	273.02	261.51	247.52	259.11	246.42	243.11	263.88	233.78	210.79
374.80748	503.20	468.83	458.89	437.07	441.28	413.64	401.70	446.06	406.36	346.66
496.72748	610.81	569.90	561.40	532.00	532.60	496.10	478.60	538.90	499.70	425.70
618.64748	714.75	672.34	661.09	623.53	622.47	577.95	557.22	632.98	592.39	510.63
699.92748	785.64	741.94	724.63	681.48	682.37	631.23	607.62	696.87	650.08	568.58
710.08748	794.39	749.60	N/A	688.69	689.51	637.75	613.10	704.89	657.20	575.83
756.6025	835.58	789.94	768.83	723.01	723.41	669.04	643.50	743.15	692.20	610.85
764.8575	842.81	796.94	775.24	729.12	729.48	674.57	648.79	750.05	698.40	617.10
773.1125	850.17	803.95	781.74	735.28	735.59	680.19	654.00	756.95	704.78	623.47
776.2875	853.13	806.82	784.36	737.73	738.03	682.40	656.24	759.68	707.26	625.98
779.4625	855.96	809.50	786.85	740.13	740.37	684.57	658.24	762.34	709.68	628.42
782.6375	858.77	812.06	789.37	742.42	742.67	686.85	660.35	764.95	712.17	630.86
785.8125	861.44	814.70	791.74	744.67	744.91	688.90	662.27	767.49	714.50	633.20
788.9875	864.35	817.56	794.45	747.12	747.36	691.21	664.46	770.31	717.12	635.80
792.1625	867.24	820.30	796.96	749.50	749.70	693.37	666.51	772.95	719.54	638.23
795.3375	869.79	823.04	799.61	751.94	752.10	695.58	668.55	775.70	722.04	640.74
798.5125	872.77	825.74	802.12	754.36	754.44	697.70	670.57	778.35	724.48	642.97

Table B4. Test 57 EAST Shock Time of Arrivals

Distance, cm	Time, μs											
	T57-8	T57-10	T57-14	T57-15	T57-16	T57-22	T57-25	T57-34	T57-36	T57-37	T57-40	T57-41
106.045	144.60	136.04	167.52	156.02	150.39	186.57	171.08	183.33	154.27	162.33	157.18	168.34
220.345	225.46	213.00	259.35	241.25	233.28	317.67	295.25	312.76	263.78	278.89	270.75	288.07
374.80748	342.18	323.31	392.48	364.70	353.50	539.95	513.14	529.86	452.63	478.49	461.13	492.71
496.72748	438.71	413.68	501.32	465.99	452.77	651.94	623.96	638.01	547.38	578.03	555.53	598.68
618.64748	541.88	509.86	615.43	573.28	558.55	764.56	726.16	744.35	639.00	677.20	649.00	706.08
699.92748	613.76	577.32	695.36	648.41	632.66	N/A	795.71	817.23	702.27	745.30	713.25	777.90
710.08748	623.09	586.15	705.83	658.25	642.60	852.66	804.33	825.98	710.14	753.64	721.20	786.40
756.6025	664.87	625.57	752.50	702.31	686.12	897.77	843.86	866.90	746.04	791.71	758.16	826.04
764.8575	672.49	632.72	761.03	710.38	694.06	905.79	850.88	874.07	752.54	798.62	764.86	833.22
773.1125	680.10	639.90	769.61	718.46	702.02	914.03	857.89	881.43	759.06	805.54	771.57	840.46
776.2875	683.16	642.74	772.90	721.62	705.13	917.17	860.65	884.18	761.75	808.23	774.22	843.27
779.4625	685.89	645.33	776.14	724.58	708.08	920.18	863.23	887.00	764.05	810.82	776.72	846.04
782.6375	689.04	648.23	779.58	727.85	711.27	923.46	866.10	889.94	766.72	813.68	779.46	848.91
785.8125	691.67	650.78	782.55	730.69	714.06	926.30	868.51	892.49	769.01	816.01	781.80	851.46
788.9875	694.89	653.79	786.06	734.03	717.38	929.69	871.47	895.47	771.75	818.97	784.59	854.47
792.1625	697.83	656.59	789.39	737.18	720.46	932.64	874.19	898.37	774.28	821.67	787.22	857.29
795.3375	700.66	659.34	792.63	740.28	723.53	935.91	876.81	901.07	776.77	824.32	789.75	860.07
798.5125	703.83	662.13	796.20	743.57	726.76	939.34	879.74	904.14	779.39	827.10	792.47	862.96

C. Appendix - Spectral Resolution Function

The ILS described in Section IV.A. for benchmark tests is given here. There are two lineshapes described. For measurements below 500 nm, the parameters are for the square root of Voigt function, where:

$$ILS_1(\Delta\lambda) = \frac{[V(\Delta\lambda; w_l, w_g)]^{0.5}}{2\int_0^\infty [V(x; w_l, w_g)]^{0.5}\mathrm{d}x} \tag{C1}$$

where the Voigt function:

$$V(\Delta\lambda; w_g, w_g) = L(\Delta\lambda; w_l) \otimes G(\Delta\lambda; w_g) \tag{C2}$$

is the convolution of Lorentzian and Gaussian functions. The Lorentzian and Gaussian functions are given as:

$$L(\Delta\lambda; w_l) = \frac{\pi^{-1}}{(\frac{\Delta\lambda}{w_l})^2 + 1} \tag{C3}$$

$$G(\Delta\lambda; w_g) = \frac{1}{w_g}\sqrt{\frac{\ln 2}{\pi}}\exp\left[-\ln 2\left(\frac{\Delta\lambda}{w_g}\right)^2\right] \tag{C4}$$

where w_g and w_l are the half-width at half-maximum. Note that the forms of L and G are normalized such that their integral is unity. The denominator in Eq. C1 indicates that the ILS must be similarly normalized. This is not expressed analytically, and must be done numerically. The parameters entering into the above expression are given in Tables C1 – C5, in units of nanometers:

Table C1. Instrument Lineshapes for Deep VUV at 0.2 Torr

Test Series	Shot Number	Velocity, km/s	w_g	w_l
57	6	10.13	0.139	0.0024
57	7	10.44	0.139	0.0024
57	8	10.66	0.139	0.0024
57	11	11.50	0.139	0.0024

Table C2. Instrument Lineshapes for VUV at 0.2 Torr

Test Series	Shot Number	Velocity, km/s	w_g	w_l
57	14	9.53	0.139	0.0024
57	15	10.12	0.139	0.0024
50	29	10.29	0.084	0.0025
57	16	10.30	0.139	0.0024
50	93	10.68	0.084	0.0025
57	37	11.79	0.139	0.0024
57	36	12.50	0.139	0.0024

Table C3. Instrument Lineshapes for VUV at 0.1 Torr

Test Series	Shot Number	Velocity, km/s	w_g	w_l
57	22	10.17	0.139	0.0024
50	115	10.44	0.084	0.0025
50	20	11.11	0.084	0.0025
57	34	11.15	0.139	0.0024
50	24	11.74	0.084	0.0025
50	107	11.86	0.084	0.0025

Table C4. Instrument Lineshapes for UV/Vis at 0.2 Torr

Test Series	Shot Number	Velocity, km/s	w_g	w_l
50	36	9.02	0.28	0.070
50	59	9.98	0.28	0.070
50	29	10.29	0.28	0.070
47	33	10.32	0.73	0.022
57	41	11.22	0.24	0.033
57	40	12.19	0.24	0.033

Table C5. Instrument Lineshapes for UV/Vis at 0.1 Torr

Test Series	Shot Number	Velocity, km/s	w_g	w_l
50	17	9.32	0.284	0.070
50	27	10.87	0.284	0.070
52	1	11.27	0.282	0.027
52	2	11.72	0.282	0.027
52	5	12.45	0.282	0.027
52	8	13.50	0.282	0.027
52	15	15.52	0.196	0.016

Above 500 nm, the second form of the ILS is preferred. This function is a linear combination of Lorentzian and Gaussian functions. The function normalization is included in the following formula:

$$ILS_2(\Delta\lambda) = \frac{G(\Delta\lambda; w_g) + 10^r L(\Delta\lambda; w_l)}{1 + 10^r} \tag{C5}$$

The corresponding parameters are as follows:

Table C6. Instrument Lineshapes for Vis/NIR at 0.2 Torr

Test Series	Shot Number	Velocity, km/s	w_g	w_l	r
50	44	8.05	1.01	2.83	-0.11
47	37	10.27	0.90	4.92	-1.01
50	30	10.92	1.01	2.83	-0.11
57	37	11.79	1.21	1.33	0.47
52	20	12.89	0.84	2.69	-0.43

Table C7. Instrument Lineshapes for Vis/NIR at 0.1 Torr

Test Series	Shot Number	Velocity, km/s	w_g	w_l	r
50	102	9.71	1.01	2.83	-0.11
50	104	10.13	1.01	2.83	-0.11
50	106	10.97	1.01	2.83	-0.11
50	105	11.26	1.01	2.83	-0.11
57	25	11.67	1.48	3.79	-0.74
52	8	13.50	1.01	2.83	-0.11
52	13	14.46	0.84	2.69	-0.43
52	15	15.52	0.84	2.69	-0.43

In the infrared, it is often not possible to fit a Lorentzian component. In this case, a single Gaussian is used for the ILS and no value is given for w_l or r in the table.

Table C8. Instrument Lineshapes for IR at 0.2 Torr

Test Series	Shot Number	Velocity, km/s	w_g	w_l	r
50	59	9.98	2.83		
50	57	10.25	1.57	8.46	-0.91
57	8	10.66	0.39	1.35	-0.02
50	97	10.81	2.83		
57	10	11.36	0.39	1.35	-0.02
52	19	11.88	2.18		
52	21	12.87	2.18		

Table C9. Instrument Lineshapes for IR at 0.1 Torr

Test Series	Shot Number	Velocity, km/s	w_g	w_l
50	104	10.13	2.83	
50	106	10.97	2.83	
50	105	11.26	2.83	
52	1	11.27	2.18	
52	2	11.72	2.18	
52	15	15.52	2.18	

D. Appendix - Spatial Resolution Function

The spatial resolution function is given as the convolution of three different functions, as follows:

$$SRF(x) = f_{opt}(x) \otimes f_{cam}(x) \otimes f_{motion}(x)$$

Detailed forms of these functions are discussed in [2]. Here we use approximated forms of these functions defined as follows. For the optics up to 900 nm, f_{opt} is given by a triangular function:

$$f_{opt}(\Delta x) = \frac{2}{d_{opt}} \max\left(1 - \frac{2|\Delta x|}{d_{opt}}, 0\right) \tag{D1}$$

The camera function is given by the same function as ILS1 in Appendix C. The motion function is given by a square wave with width equal to the product of velocity and gating time.

$$f_{motion}(\Delta x) = \begin{cases} d_{gate}^{-1} & |\Delta x| < d_{gate}/2 \\ 0 & |\Delta x| > d_{gate}/2 \end{cases} \tag{D2}$$

Values for d_{gate}, d_{opt} and w_g, w_l are given in Tables D1 – D7 for these three cameras below, in units of cm.

Table D1. Spatial Resolution Functions for Deep VUV at 0.2 Torr

Test Series	Shot Number	Velocity, km/s	d_{opt}	w_g	w_l	d_{gate}
57	6	10.13	0.041	0.061	0.002	0.253
57	7	10.44	0.041	0.066	0.001	0.261
57	8	10.66	0.041	0.067	0.001	0.267
57	11	11.50	0.041	0.081	0.001	0.287

Table D2. Spatial Resolution Functions for VUV at 0.1 Torr

Test Series	Shot Number	Velocity, km/s	d_{opt}	w_g	w_l	d_{gate}
57	22	10.17	0.041	0.064	0.001	0.254
50	115	10.44	0.041	0.042	0.003	0.522
50	20	11.11	0.041	0.057	0.000	0.555
57	34	11.15	0.041	0.063	0.004	0.279
50	24	11.74	0.041	0.060	0.000	0.587
50	107	11.86	0.041	0.036	0.005	0.593

Table D3. Spatial Resolution Functions for VUV at 0.1 Torr

Test Series	Shot Number	Velocity, km/s	d_{opt}	w_g	w_l	d_{gate}
57	14	9.53	0.041	0.068	0.001	0.238
57	15	10.12	0.041	0.064	0.002	0.253
50	29	10.29	0.041	0.026	0.063	0.514
57	16	10.30	0.041	0.063	0.001	0.258
50	93	10.68	0.041	0.112	0.007	1.068
57	37	11.79	0.041	0.061	0.007	0.295
57	36	12.50	0.041	0.057	0.004	0.313

Table D4. Spatial Resolution Functions for UV/Vis at 0.1 Torr

Test Series	Shot Number	Velocity, km/s	d_{opt}	w_g	w_l	d_{gate}
50	36	9.02	0.041	0.018	0.006	0.226
50	59	9.98	0.041	0.028	0.003	0.499
50	29	10.29	0.041	0.021	0.004	0.257
47	33	10.32		TBD		
57	41	11.22	0.041	0.057	0.005	0.112
57	40	12.19	0.041	0.056	0.004	0.122

Table D5. Spatial Resolution Functions for UV/Vis at 0.1 Torr

Test Series	Shot Number	Velocity, km/s	d_{opt}	w_g	w_l	d_{gate}
50	17	9.32	0.041	0.021	0.002	0.233
50	27	10.87	0.041	0.023	0.002	0.272
52	1	11.27	0.041	0.016	0.003	0.282
52	2	11.72	0.041	0.016	0.003	0.293
52	5	12.45	0.041	0.016	0.003	0.311
52	8	13.50	0.041	0.018	0.003	0.338
52	15	15.52	0.041	0.018	0.003	0.388

Table D6. Spatial Resolution Functions for Vis/NIR at 0.1 Torr

Test Series	Shot Number	Velocity, km/s	d_{opt}	w_g	w_l	d_{gate}
50	44	8.05	0.041	0.047	0.013	0.201
47	37	10.27		TBD		
50	30	10.92	0.041	0.063	0.015	0.109
57	37	11.79	0.041	0.072	0.002	0.118
52	20	12.89	0.041	0.022	0.006	0.129

Table D7. Spatial Resolution Functions for Vis/NIR at 0.1 Torr

Test Series	Shot Number	Velocity, km/s	d_{opt}	w_g	w_l	d_{gate}
50	102	9.71	0.041	0.025	0.007	0.097
50	104	10.13	0.041	0.023	0.009	0.101
50	106	10.97	0.041	0.024	0.008	0.110
50	105	11.26	0.041	0.025	0.007	0.113
57	25	11.67	0.041	0.052	0.005	0.117
52	8	13.50	0.041	0.020	0.006	0.135
52	13	14.46	0.041	0.022	0.006	0.145
52	15	15.52	0.041	0.022	0.007	0.155

For the infrared camera, the optical function is taken to be a trapezoid :

$$f_{opt}(\Delta x) = \frac{2d_{opt,2}}{d_{opt,2}^2 - d_{opt,1}^2} \min\left(1 - \frac{d_{opt,1}}{d_{opt,2}}, \max\left(1 - \frac{2|\Delta x|}{d_{opt,2}}\right), 0\right) \tag{D3}$$

where $d_{opt,1}$ and $d_{opt,2}$ are the two bases of the trapezoid. The camera shape is taken to be a Gaussian with half-width w_g. Values of d_{opt}, d_{gate} and w_g for the infrared cameras are given in Tables D8 and D9.

Table D8. Spatial Resolution Functions for IR at 0.1 Torr

Test Series	Shot Number	Velocity, km/s	d_{opt1}	d_{opt2}	w_g	d_{gate}
50	59	9.98	0.313	0.128	0.140	0.499
50	57	10.25	0.313	0.128	0.141	0.513
57	8	10.66	0.313	0.128	0.119	1.045
50	97	10.81	0.313	0.128	0.132	1.081
57	10	11.36	0.313	0.128	0.116	1.113
52	19	11.88	0.313	0.128	0.068	1.188
52	21	12.87	0.313	0.128	0.072	1.287

Table D9. Spatial Resolution Functions for IR at 0.1 Torr

Test Series	Shot Number	Velocity, km/s	d_{opt1}	d_{opt2}	w_g	d_{gate}
50	104	10.13	0.313	0.128	0.103	1.013
50	106	10.97	0.313	0.128	0.095	1.097
50	105	11.26	0.313	0.128	0.085	1.126
52	1	11.27	0.313	0.128	0.111	1.127
52	2	11.72	0.313	0.128	0.111	1.172
52	15	15.52	0.313	0.128	0.075	1.552